Frontiers of Information Technology & Electronic Engineering
www.jzus.zju.edu.cn; engineering.cae.cn; www.springerlink.com
ISSN 2095-9184 (print); ISSN 2095-9230 (online)
E-mail: jzus@zju.edu.cn

Transmission design for the XL-RIS-aided massive MIMO system with visibility regions#

Luchu LI[1], Cunhua PAN‡[1], Kangda ZHI[2], Hong REN[1]

[1]*School of Information Science and Engineering, Southeast University, Nanjing 210096, China*

[2]*School of Electrical Engineering and Computer Science, Technical University of Berlin, Berlin 10623, Germany*

E-mail: 213203234@seu.edu.cn; cpan@seu.edu.cn; k.zhi@tu-berlin.de; hren@seu.edu.cn

Received May 10, 2024; Revision accepted Oct. 27, 2024; Crosschecked Dec. 11, 2024

Abstract: This study proposes a two-timescale transmission scheme for extremely large-scale reconfigurable intelligent surface aided (XL-RIS-aided) massive multi-input multi-output (MIMO) systems in the presence of visibility regions (VRs). The beamforming of base stations (BSs) is designed based on rapidly changing instantaneous channel state information (CSI), while the phase shifts of RIS are configured based on slowly varying statistical CSI. Specifically, we first formulate a system model with spatially correlated Rician fading channels and introduce the concept of VRs. Then, we derive a closed-form approximate expression for the achievable rate and analyze the impact of VRs on system performance and computational complexity. Then, we solve the problem of maximizing the minimum user rate by optimizing the phase shifts of RIS through an algorithm based on accelerated gradient ascent. Finally, we present numerical results to validate the performance of the considered system from different aspects and reveal the low system complexity of deploying XL-RIS in massive MIMO systems with the help of VRs.

Key words: Reconfigurable intelligent surface; Massive multi-input multi-output (MIMO); Two-timescale transmission scheme; Visibility regions

https://doi.org/10.1631/FITEE.2400375 **CLC number:** TN928

1 Introduction

Recently, reconfigurable intelligent surface (RIS), also known as intelligent reflecting surface (IRS), has been extensively studied by academia and industry and has been recognized as an appealing complementary technology for next-generation communication systems (Pan et al., 2021; Liu et al., 2023; Zhang Y, 2023). It is an array composed of a large number of reconfigurable subwavelength units, which can achieve signal enhancement, attenuation, focusing, scattering, and other functions. Specifically, each RIS element can independently induce changes in the amplitude and phase of the incident signal, allowing the reflected signal to be constructively added to signals from other paths. Therefore, it can customize the wireless environment by manually controlling electromagnetic (EM) waves, thereby improving spectrum efficiency. Meanwhile, RIS can significantly improve the performance, especially when direct links between users and base stations (BSs) are obstructed. Therefore, compared to existing multi-antenna systems, RIS has the potential to achieve better performance while reducing costs and energy consumption.

In recent years, many researchers have studied the application of RIS in wireless systems from different perspectives. The free-space path-loss models

‡ Corresponding author

Electronic supplementary materials: The online version of this article (https://doi.org/10.1631/FITEE.2400375) contains supplementary materials, which are available to authorized users

ORCID: Luchu LI, https://orcid.org/0009-0006-4977-1254; Cunhua PAN, https://orcid.org/0000-0001-5286-7958; Kangda ZHI, https://orcid.org/0000-0002-1677-847X; Hong REN, https://orcid.org/0000-0002-3477-1087

for RIS-assisted wireless communications were developed for different scenarios by studying the physics and EM nature of RISs (Tang et al., 2021). Pan et al. (2022) provided a comprehensive overview of recent advances in RIS/IRS-aided wireless systems from the signal processing perspective. Xu et al. (2023) studied the energy efficiency of a RIS-assisted multi-cell communication system with a realistic RIS power consumption model and optimized the transmit beamforming vectors at the BS by a proposed alternative optimization algorithm. By jointly optimizing the beamforming matrix at amplify-and-forward (AF) relay and the phase-shift matrix at RIS, Wang XH et al. (2023) proposed a RIS-aided AF relay network, and two schemes were put forward to address a maximizing signal-to-noise ratio (SNR) problem.

Recently, the supporting technologies of applying RIS in various scenarios have also been investigated in a wide range. Specifically, a novel cascaded channel estimation strategy with low pilot overhead was proposed by exploiting the sparsity and the correlation of multi-user (MU) cascaded channels in millimeter-wave (mmWave) multi-input single-output (MISO) systems (Zhou G et al., 2022). Peng et al. (2023) proposed a novel two-stage uplink channel estimation strategy with reduced pilot overhead and error propagation for RIS-aided MU mmWave multi-antenna systems. Jiang et al. (2023) proposed a three-dimensional (3D) physics-based double-RIS cooperatively-assisted multi-input multi-output (MIMO) stochastic channel model for unmanned aerial vehicle (UAV)-to-ground communication scenarios. Yang L et al. (2020a) modeled the statistical distribution of the RIS-assisted ground-to-air (G2A) links and proved that the use of RISs can effectively improve the coverage and reliability of UAV communication systems. Ren et al. (2023) derived the approximate expression of the sum achievable security data rate (ASDR) with statistical channel state information (CSI) and demonstrated the effectiveness of using RIS in improving security performance.

Furthermore, researchers have conducted numerous studies and improvements on RIS-aided systems to meet the different needs of actual environments. A more efficient channel estimator was developed by leveraging the unitary approximate message passing (UAMP), which facilitates the applications of existing algorithms to a general RIS-aided MIMO system with a larger number of reflecting elements (Guo et al., 2023). Considering radio frequency damage and phase noise, Zhou SQ et al. (2020) conducted a theoretical study on the fundamental trade-off between spectrum and energy efficiency of RIS communication networks. In Chen et al. (2024), a model-free cross-entropy algorithm was proposed to optimize the binary RIS configuration for improving the SNR at the receiver. Huang et al. (2020) demonstrated that holographic RIS can become an attractive way of achieving high spatial resolutions in satellite networks. Yang L et al. (2020b) studied the secrecy performance of a RIS-aided wireless communication system in the presence of an eavesdropping user. Zheng et al. (2021) presented a double-RIS cooperatively-assisted MIMO communication system where two distributed RISs were deployed near a user group and a multi-antenna BS, separately. Assuming that the RIS with the highest instantaneous end-to-end SNR was selected to aid the communication, Yang L et al. (2021) considered a network assisted by multiple RISs and investigated the outage probability and average sum rate.

Although the advantages of the RIS have been demonstrated in the aforementioned studies, most of them were built on the assumption of estimating instantaneous CSI in each channel coherent interval. However, in practice, transmission design schemes based on instantaneous CSI face two challenges (Zhi et al., 2023). The RIS usually includes a large number of reflecting elements to achieve the desired gains. However, the pilot overhead of channel estimation schemes may increase in proportion to the number of RIS elements (Wang ZR et al., 2020), leading to excessive pilot overhead. Then, designing algorithms based on instantaneous CSI requires frequent beamforming calculations and information feedback, resulting in high computational complexity, feedback overhead, and energy consumption.

To address the above issues, researchers are currently considering adopting a two-timescale scheme to make the application of RIS more practical. Specifically, in a two-timescale scheme, BS beamforming is designed based on instantaneous aggregated CSI, while optimization of RIS parameters is only decided based on long-term statistical CSI, such as position and angle information (Zhi, 2023; Zhi et al., 2023). As a result, it is only necessary to

update the phase shift of RIS components when the statistical CSI changes (Han et al., 2019). Specifically, Jia et al. (2020) and Han et al. (2019) studied RIS-aided single-user communication systems by taking into consideration interference and non-interference, respectively. Abrardo et al. (2021) considered a multi-RIS MU MIMO system and optimized the phase shifts of RIS elements, as well as beamforming vectors at BSs and user devices, without the need for instantaneous CSI or second-order channel statistics, to maximize the user rate. Gao et al. (2021) proposed an effective passive reflection beamforming design for the RIS, which uses statistical CSI to analyze the achievable rate of the network while considering the impact of CSI estimation errors. Hu et al. (2021) proposed a two-timescale channel estimation framework and a dual-link pilot transmission scheme, where the BS transmits downlink pilots and receives uplink pilots reflected by the RIS. To maximize the average achievable rate of RIS-assisted MIMO systems, Cao et al. (2022) presented a new two-timescale beamforming approach, where the RIS was configured relatively infrequently based on statistical CSI, and the BS precoder and power allocation were updated frequently based on quickly outdated instantaneous CSI. In the presence of spatial correlation and electromagnetic interference (EMI), Zhi et al. (2023) investigated the two-timescale transmission scheme for RIS-aided MIMO systems. For cell-free systems, a low-complexity algorithm via the two-timescale transmission protocol was proposed by Gan et al. (2022), where the joint beamforming at BSs and RISs was designed via an alternating optimization framework. By using the active RIS architecture, a MU two-timescale channel estimation protocol was proposed to minimize the pilot overhead in Yang SJ et al. (2023).

As massive MIMO technology was commercially deployed in the fifth-generation (5G) communication systems, a useful complementary is to deploy extremely large-scale (XL) passive reflection arrays into massive MIMO systems (Han et al., 2022). This is because, thanks to the low-cost feature, the size of a RIS can be made very large to extend the service region, which can compensate for the double-fading effect (Zhi et al., 2022a), and also achieve better performance in terms of localization and communication. Besides, XL-RIS can achieve unprecedented gains in spatial multiplexing, SNR, energy efficiency, and coverage probability with the help of a larger array aperture and a stronger ability to customize the wireless environment. However, with a larger aperture, the users could be easily located in the near field of the XL-RIS, based on the Rayleigh distance that characterizes the near-field region. As a result, the practical spherical EM wavefront can no longer be approximated as the tractable planar wavefront (Zhi et al., 2024). Moreover, the channel between users and XL-RIS will show spatial non-stationarity due to the non-stationary power distribution in the near-field channel because of the obstacles in the complicated environment (Carvalho et al., 2020). Specifically, as unequal path loss is experienced by different RIS elements and some RIS elements suffer from blockage caused by obstacles, the received signal power from users on the XL-RIS will be concentrated on a portion of the RIS elements, which is indicated by the visibility region (VR) (Han et al., 2022). As a result, it is necessary to revise typical channel models and algorithms to capture spatially non-stationary fading and other near-field features in XL-RIS-aided massive MIMO systems (Li XR et al., 2015; Carvalho et al., 2020).

Taking the existence of VR into consideration, Cui and Dai (2022) proposed a polar simultaneous orthogonal matching pursuit (OMP) algorithm for near-field channel estimation in XL-MIMO systems. Ali et al. (2019) proposed a simple non-stationary channel model with VRs and analyzed the performance of conjugate beamforming and zero-forcing precoding in the downlink MU XL-MIMO systems. Considering the non-stationarity between the RIS and users, Han et al. (2022) proposed a recognition module that can estimate the VR of each user with line-of-sight (LoS) components between the RIS and users. For XL-RIS-aided systems, Wei et al. (2022) proposed a low-cost near-field beam training scheme. Yu et al. (2023) studied the channel estimation problem of XL-RIS-aided mmWave communication systems considering near-field effects and spatially non-stationary effects. Gunasinghe and Amarasuriya (2023) investigated the achievable rate of XL-RIS-aided downlink massive MIMO systems in the presence of the whole/partial VRs, spatial correlation, and imperfectly estimated CSI.

However, in most of the aforementioned studies, the focus was on channel estimating and spatially non-stationary effects caused by XL-MIMO

systems. Moreover, Jia et al. (2020) and Yang SJ et al. (2023) did not consider the employment of XL-RIS and ignored the VRs of users. To the best of our knowledge, there are few studies on the performance analysis and phase shift design of spatially non-stationary XL-RIS-assisted massive MIMO systems based on two-timescale schemes, and therefore the performance and potential deserve further investigation.

To fill this research gap, in this study, we analyze the uplink two-timescale transmission scheme of XL-RIS-assisted massive MIMO systems in the presence of VRs, considering the spatially non-stationary effects caused by XL-RIS, and apply the general Rician channel model to evaluate the impact of LoS and non-LoS (NLoS) channel components. Our study can be generalized to the case with multiple antenna users, and its difficulty lies mainly in the increase of the channel matrix dimension (Wang JH et al., 2021; Li RW et al., 2023), but the methods and algorithm are still applicable. The main contributions of the study are summarized as follows:

1. By employing the low-complexity maximal-ratio-combining (MRC) detector at the BS, we derive a closed-form expression of the uplink achievable rate under the correlated Rician channel model in the presence of VRs. This expression can be applied to any finite numbers of RIS elements and BS antennas and depends only on the statistical CSI. Then, we analyze the impact of VRs and assess how they help reduce computational complexity.

2. Based on the derived expression, we formulate a problem of maximizing the minimum user rate with statistical CSI. Then, an effective algorithm is proposed to design the phase shifts of the XL-RIS based on accelerated gradient ascent.

3. To unveil the property and benefit of integrating XL-RIS into massive MIMO networks, we provide simulation results about various important parameters. The results reveal that the existence of VR leads to a decrease in performance while the exploitation of its properties is beneficial in reducing the computational complexity of the system. Besides, it is shown that the proposed gradient algorithm can effectively solve the RIS phase optimization problem and has higher efficiency compared to the genetic algorithm (GA).

Notations: The transpose, conjugate transpose, and inverse of matrix $\boldsymbol{X}$ are denoted by $\boldsymbol{X}^{\mathrm{T}}$, $\boldsymbol{X}^{\mathrm{H}}$, and $\boldsymbol{X}^{-1}$, respectively. $[\boldsymbol{X}]_{m,n}$ denotes the $(m,n)^{\mathrm{th}}$ entry of matrix $\boldsymbol{X}$. The real, trace, expectation, and covariance operators are denoted by $\mathrm{Re}\{\cdot\}$, $\mathrm{Tr}(\cdot)$, $\mathbb{E}\{\cdot\}$, and $\mathrm{Cov}\{\cdot\}$, respectively. The operator mod returns the remainder after division, and $\lfloor x \rfloor$ denotes the nearest integer smaller than x.

2 System model

As shown in Fig. 1, we consider a typical XL-RIS-aided massive MIMO communication system with one BS, one XL-RIS, and K single-antenna users. The BS and XL-RIS are equipped with M antennas and $N = N_1 \times N_2$ passive reflecting elements, using uniform linear array (ULA) and uniform planar array (UPA) models (N_1 rows and N_2 columns), respectively. The RIS is connected to the BS through a dedicated transmission link. Due to potential obstructions such as buildings and other objects, we assume that the direct link from the BS to users may be blocked (Zheng et al., 2021).

Considering that the RIS can be mounted on tall building walls, it can help create channels dominated by LoS propagation with a few scatterers (Zhi et al., 2022b). Thus, we adopt the Rician fading model for the channel between the BS and the RIS and the channels between users and the RIS (Jia et al., 2020). We denote $\boldsymbol{H}_2 \in \mathbb{C}^{M\times N}$ and $\boldsymbol{H}_1 = [\boldsymbol{h}_1, \boldsymbol{h}_2, \ldots, \boldsymbol{h}_K] \in \mathbb{C}^{N\times K}$ as the channel between the BS and RIS, and the channels between

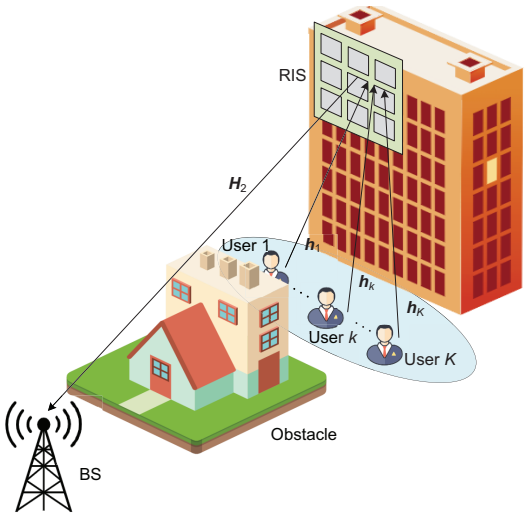

Fig. 1 An XL-RIS-aided massive MIMO system (XL: extremely large-scale; RIS: reconfigurable intelligent surface; MIMO: multi-input multi-output; BS: base station)

the RIS and users, respectively. Specifically, these channels can be modeled as follows:

$$\boldsymbol{h}_k=\sqrt{\alpha_k}\left(\sqrt{\frac{\varepsilon_k}{\varepsilon_k+1}}\boldsymbol{D}_k^{1/2}\bar{\boldsymbol{h}}_k+\sqrt{\frac{1}{\varepsilon_k+1}}\boldsymbol{R}_{\mathrm{VR},k}^{1/2}\tilde{\boldsymbol{h}}_k\right), \tag{1}$$

$$\boldsymbol{H}_2=\sqrt{\beta}\left(\sqrt{\frac{\delta}{\delta+1}}\bar{\boldsymbol{H}}_2+\sqrt{\frac{1}{\delta+1}}\tilde{\boldsymbol{H}}_2\boldsymbol{R}_{\mathrm{ris}}^{1/2}\right), \tag{2}$$

where α_k and β represent the large-scale path-loss factors of the user k–RIS link and BS–RIS link, respectively. ε_k and δ are the Rician factors of the user k–RIS link and the BS–RIS link, respectively. $\boldsymbol{D}_k$ denotes the visibility indicator matrix. $\boldsymbol{R}_{\mathrm{ris}}$ and $\boldsymbol{R}_{\mathrm{VR},k}$ are the spatial correlation matrices of the RIS and VRs, respectively. In addition, $\bar{\boldsymbol{h}}_k$ and $\bar{\boldsymbol{H}}_2$ denote the LoS components, while $\tilde{\boldsymbol{h}}_k$ and $\tilde{\boldsymbol{H}}_2$ denote the NLoS components.

For the NLoS components, $\tilde{\boldsymbol{h}}_k$ and $\tilde{\boldsymbol{H}}_2$ are independent and identically distributed (i.i.d.) complex Gaussian random variables with zero mean and unit variance. First, we denote that $\varphi_{kr}^{\mathrm{a}}$ and $\varphi_{kr}^{\mathrm{e}}$ are the azimuth and elevation angles of arrival (AoAs) at the RIS from user k, respectively, and $\varphi_{\mathrm{t}}^{\mathrm{a}}$ and $\varphi_{\mathrm{t}}^{\mathrm{e}}$ are the azimuth and elevation angles of departure (AoDs) toward the BS from the RIS, respectively. $\phi_{\mathrm{r}}^{\mathrm{a}}$ and $\phi_{\mathrm{r}}^{\mathrm{e}}$ are the azimuth and elevation AoAs at the BS from the RIS, respectively. Besides, we assume that these angles can be calculated by using the locations obtained from the Global Positioning System (GPS) (Zhi et al., 2022b). Then, for the LoS components, $\bar{\boldsymbol{h}}_k$ and $\bar{\boldsymbol{H}}_2$ are modeled as follows (Zhi et al., 2024):

$$[\bar{\boldsymbol{h}}_k]_l=\sqrt{\varepsilon_k}\exp\{-\mathrm{j}[\chi_k]_l\}, \tag{3}$$

$$\bar{\boldsymbol{H}}_2=\boldsymbol{a}_M(\phi_{\mathrm{r}}^{\mathrm{a}},\phi_{\mathrm{r}}^{\mathrm{e}})\boldsymbol{a}_N^{\mathrm{H}}(\varphi_{\mathrm{t}}^{\mathrm{a}},\varphi_{\mathrm{t}}^{\mathrm{e}}), \tag{4}$$

where

$$[\chi_k]_l\approx\frac{2\pi}{\lambda}\cdot\sqrt{(x(l)d_{\mathrm{H}}-u_{k,x})^2+(y(l)d_{\mathrm{V}}-u_{k,y})^2+u_{k,z}^2},$$

and d_{H} and d_{V} denote the height and width of a single RIS element, respectively, which can be assumed to be $d_{\mathrm{H}}=d_{\mathrm{V}}=d_{\mathrm{ris}}$. $x(l)$ and $y(l)$ are the horizontal and vertical indices of element l, respectively, on the two-dimensional grid. $u_{k,x}=r_{k,o}\sin\varphi_{kr}^{\mathrm{e}}\cos\varphi_{kr}^{\mathrm{a}}$, $u_{k,y}=r_{k,o}\sin\varphi_{kr}^{\mathrm{e}}\sin\varphi_{kr}^{\mathrm{a}}$, and $u_{k,z}=r_{k,o}\cos\varphi_{kr}^{\mathrm{e}}$ are the x-, y-, and z-axis coordinates of user k, respectively, where $r_{k,o}$ is the distance from user k to the XL-RIS. In addition, let $\boldsymbol{a}_X(\vartheta^{\mathrm{a}},\vartheta^{\mathrm{e}})\in\mathbb{C}^X$ represent the array response vector, where the x^{th} term is as follows:

$$\begin{aligned}&[\boldsymbol{a}_M(\vartheta^{\mathrm{a}},\vartheta^{\mathrm{e}})]_x=\exp\left[\mathrm{j}2\pi\frac{d_{\mathrm{bs}}}{\lambda}(x-1)\sin\vartheta^{\mathrm{e}}\sin\vartheta^{\mathrm{a}}\right],\\&[\boldsymbol{a}_N(\vartheta^{\mathrm{a}},\vartheta^{\mathrm{e}})]_x\\&=\exp\left\{\mathrm{j}2\pi\frac{d_{\mathrm{ris}}}{\lambda}\left[\lfloor(x-1)/\sqrt{N}\rfloor\sin\vartheta^{\mathrm{e}}\sin\vartheta^{\mathrm{a}}\right.\right.\\&\left.\left.+\left((x-1)\bmod\sqrt{N}\right)\cos\vartheta^{\mathrm{e}}\right]\right\}.\end{aligned} \tag{5}$$

Here, d_{bs}, d_{ris}, and λ represent the BS antenna spacing, RIS element spacing, and wavelength, respectively. To simplify the symbols, in the rest of the study, $\boldsymbol{a}_M(\phi_{\mathrm{r}}^{\mathrm{a}},\phi_{\mathrm{r}}^{\mathrm{e}})$ and $\boldsymbol{a}_N(\varphi_{\mathrm{t}}^{\mathrm{a}},\varphi_{\mathrm{t}}^{\mathrm{e}})$ are simply denoted as $\boldsymbol{a}_M$ and $\boldsymbol{a}_N$, respectively.

As shown in Fig. 2, the elements of the RIS are indexed row by row. We denote $\boldsymbol{u}_l$ as the location of the l^{th} element with respect to the origin in Fig. 2, which can be represented by the following model (Björnson and Sanguinetti, 2021):

$$\boldsymbol{u}_l=[x(l)d_{\mathrm{H}},y(l)d_{\mathrm{V}},0]^{\mathrm{T}}, \tag{6}$$

$$x(l)=\mathrm{mod}(l-1,N_2), \tag{7}$$

$$y(l)=\lfloor(l-1)/N_2\rfloor. \tag{8}$$

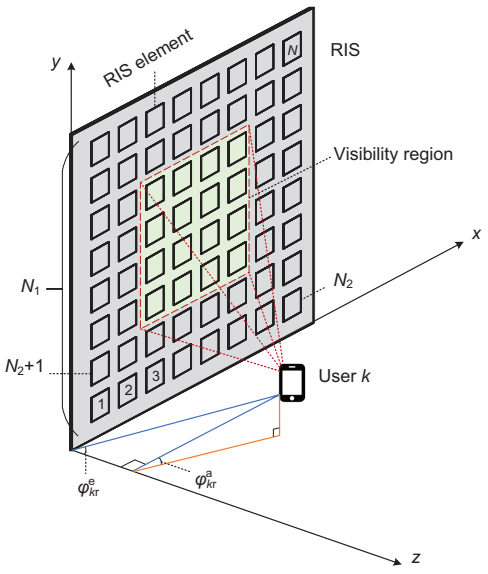

Fig. 2 Three-dimensional geometry of an XL-RIS consisting of N_2 elements per row and N_1 elements per column, in the presence of VR (XL: extremely large-scale; RIS: reconfigurable intelligent surface; VR: visibility region)

Therefore, the elements inside the spatial correlation matrix of the RIS can be defined as follows:

$$[\boldsymbol{R}_{\mathrm{ris}}]_{l,q}=\operatorname{sinc}\left(\frac{2\left\|\boldsymbol{u}_l-\boldsymbol{u}_q\right\|}{\lambda}\right),\ l,q=1,2,\ldots,N, \tag{9}$$

where $\|\boldsymbol{u}_l-\boldsymbol{u}_q\|$ represents the distance between the l^{th} and q^{th} elements of the RIS. As illustrated in Fig. 2, we use VRs to capture spatially non-stationary fading characteristics. The visibility indicator matrix $\boldsymbol{D}_k\in\mathbb{C}^{N\times N}$ is defined as follows:

$$\boldsymbol{D}_k=\operatorname{diag}(\boldsymbol{d}_k), \tag{10}$$

$$[\boldsymbol{d}_k]_n=\begin{cases}1, & \text{if } n\in\tau_k,\\ 0, & \text{otherwise.}\end{cases} \tag{11}$$

Here, $\boldsymbol{d}_k\in\mathbb{C}^N$ is the visibility indicator vector. τ_k is a set containing the indices of RIS elements, which are visible to the k^{th} user. When n belongs to τ_k, we set $[\boldsymbol{d}_k]_n$ to 1 and 0 otherwise, which did not change the range of n values. Then, the RIS covariance matrix for the k^{th} user with partial visibility is defined as follows (Ali et al., 2019):

$$\boldsymbol{R}_{\mathrm{VR},k}=\boldsymbol{D}_k^{1/2}\boldsymbol{R}_{\mathrm{ris}}\boldsymbol{D}_k^{1/2}. \tag{12}$$

With the help of XL-RIS, the received signal at the BS can be expressed as follows:

$$\boldsymbol{y}=\sqrt{p}\boldsymbol{Q}\boldsymbol{x}+\boldsymbol{n}, \tag{13}$$

where p is the average transmit power of each user. $\boldsymbol{x}=[x_1,x_2,\ldots,x_K]^{\mathrm{T}}$ represents the information sequence from K users, satisfying $\mathbb{E}\{|x_k|^2\}=1$. $\boldsymbol{n}\sim\mathcal{CN}(\boldsymbol{0},\sigma^2\boldsymbol{I}_M)$ is the additive white Gaussian noise (AWGN). $\boldsymbol{Q}\triangleq\boldsymbol{H}_2\boldsymbol{\Phi}\boldsymbol{H}_1\in\mathbb{C}^{M\times K}$ is the total aggregation channel from the K users to the BS.

We adopt the low-complexity MRC technique, due to its simple construction and near-optimal performance for massive MIMO (Marzetta et al., 2016). The BS performs MRC by multiplying the received signal $\boldsymbol{y}$ with $\boldsymbol{Q}^{\mathrm{H}}$, as follows:

$$\boldsymbol{r}_{\mathrm{VR}}=\boldsymbol{Q}^{\mathrm{H}}\boldsymbol{y}=\sqrt{p}\boldsymbol{Q}^{\mathrm{H}}\boldsymbol{Q}\boldsymbol{x}+\boldsymbol{Q}^{\mathrm{H}}\boldsymbol{n}. \tag{14}$$

Before calculating the achievable rate, the signal of user k can be written as follows:

$$r_{\mathrm{VR},k}=\sqrt{p}\boldsymbol{q}_k^{\mathrm{H}}\boldsymbol{q}_k x_k+\sqrt{p}\sum_{i=1,i\neq k}^{K}\boldsymbol{q}_k^{\mathrm{H}}\boldsymbol{q}_i x_i+\boldsymbol{q}_k^{\mathrm{H}}\boldsymbol{n}, \tag{15}$$

where $\boldsymbol{q}_k\triangleq\boldsymbol{H}_2\boldsymbol{\Phi}\boldsymbol{h}_k\in\mathbb{C}^M$ is the k^{th} column of $\boldsymbol{Q}$ denoting the cascaded channel from user k to the BS. Specifically, $\boldsymbol{q}_k$ can be represented as follows:

$$\begin{aligned}\boldsymbol{q}_k=&\boldsymbol{H}_2\boldsymbol{\Phi}\boldsymbol{h}_k\\ =&\sqrt{c_k\delta\varepsilon_k}\left(\bar{\boldsymbol{H}}_2\boldsymbol{\Phi}\boldsymbol{D}_k^{1/2}\bar{\boldsymbol{h}}_k\right)+\sqrt{c_k\delta}\left(\bar{\boldsymbol{H}}_2\boldsymbol{\Phi}\boldsymbol{R}_{\mathrm{VR},k}^{1/2}\tilde{\boldsymbol{h}}_k\right)\\ &+\sqrt{c_k\varepsilon_k}\left(\tilde{\boldsymbol{H}}_2\boldsymbol{R}_{\mathrm{ris}}^{1/2}\boldsymbol{\Phi}\boldsymbol{D}_k^{1/2}\bar{\boldsymbol{h}}_k\right)\\ &+\sqrt{c_k}\left(\tilde{\boldsymbol{H}}_2\boldsymbol{R}_{\mathrm{ris}}^{1/2}\boldsymbol{\Phi}\boldsymbol{R}_{\mathrm{VR},k}^{1/2}\tilde{\boldsymbol{h}}_k\right),\end{aligned} \tag{16}$$

where $c_k\triangleq\dfrac{\beta\alpha_k}{(\delta+1)(\varepsilon_k+1)}$, $\boldsymbol{\Phi}=\operatorname{diag}\left(\mathrm{e}^{\mathrm{j}\theta_1},\mathrm{e}^{\mathrm{j}\theta_2},\ldots,\mathrm{e}^{\mathrm{j}\theta_N}\right)$ denotes the phase shift matrix of the RIS, and $\theta_n\in[0,2\pi)$ denotes the phase shift introduced by the n^{th} RIS element.

Due to the ergodic channel, we can express the uplink achievable rate of user k as $\mathrm{RATE}_{\mathrm{VR},k}=\mathbb{E}\left\{\log_2\left(1+\mathrm{SINR}_k\right)\right\}$, and the signal-to-interference plus noise ratio (SINR) of user k is given as follows (Zhang Q et al., 2013):

$$\mathrm{SINR}_k=\frac{p\|\boldsymbol{q}_k\|^4}{\sum\limits_{i=1,i\neq k}^{K}p|\boldsymbol{q}_k^{\mathrm{H}}\boldsymbol{q}_i|^2+\sigma^2\|\boldsymbol{q}_k\|^2}. \tag{17}$$

3 Achievable rate analysis

Considering the VRs, the approximate closed-form expression of the achievable rate in the XL-RIS-aided massive MIMO system is derived and analyzed in this section. We also present the expression with reduced dimensions using the features of VRs.

Theorem 1 In the XL-RIS-aided massive MIMO system, the uplink ergodic achievable rate of user k can be approximated as follows:

$$\begin{aligned}&\mathrm{RATE}_{\mathrm{VR},k}\\ \approx&\mathbb{E}\left\{\log_2\left[\frac{pE_{\mathrm{VR},k}^{\mathrm{signal}}(\boldsymbol{\Phi})}{p\sum\limits_{i=1,i\neq k}^{K}I_{\mathrm{VR},ki}(\boldsymbol{\Phi})+\sigma^2E_{\mathrm{VR},k}^{\mathrm{noise}}(\boldsymbol{\Phi})}+1\right]\right\},\end{aligned} \tag{18}$$

where $E_{\mathrm{VR},k}^{\mathrm{signal}}(\boldsymbol{\Phi})$, $I_{\mathrm{VR},ki}(\boldsymbol{\Phi})$, and $E_{\mathrm{VR},k}^{\mathrm{noise}}(\boldsymbol{\Phi})$ are the desired signal received by the BS, the MU interference, and the thermal noise, respectively. The values of $E_{\mathrm{VR},k}^{\mathrm{noise}}(\boldsymbol{\Phi})$, $E_{\mathrm{VR},k}^{\mathrm{signal}}(\boldsymbol{\Phi})$, and $I_{\mathrm{VR},ki}(\boldsymbol{\Phi})$ are given in

$$E_{\mathrm{VR},k}^{\mathrm{noise}}(\boldsymbol{\Phi}) = c_k\left(M\delta\varepsilon_k|f_k(\boldsymbol{\Phi})|^2 + \delta f_{k,1,1}(\boldsymbol{\Phi}) + \varepsilon_k f_{kk,2}(\boldsymbol{\Phi})M + f_{k,3,1}(\boldsymbol{\Phi})M\right). \tag{19}$$

$$\begin{aligned}E_{\mathrm{VR},k}^{\mathrm{signal}}(\boldsymbol{\Phi}) =& M^2(c_k\delta\varepsilon_k)^2|f_k(\boldsymbol{\Phi})|^4 + (c_k\delta)^2\left(f_{kk,1,2}(\boldsymbol{\Phi}) + |f_{k,1,1}(\boldsymbol{\Phi})|^2\right) + (c_k\varepsilon_k)^2M(M+1)|f_{kk,2}(\boldsymbol{\Phi})|^2\\ &+ c_k^2M(M+1)\left(f_{kk,3,2}(\boldsymbol{\Phi}) + |f_{k,3,1}(\boldsymbol{\Phi})|^2\right) + 4M(c_k\delta)^2\varepsilon_k|f_k(\boldsymbol{\Phi})|^2f_{k,1,1}(\boldsymbol{\Phi})\\ &+ 2M(M+1)(c_k\varepsilon_k)^2\delta|f_k(\boldsymbol{\Phi})|^2f_{kk,2}(\boldsymbol{\Phi}) + 2M(M+1)c_k^2\delta\varepsilon_k|f_k(\boldsymbol{\Phi})|^2f_{k,3,1}(\boldsymbol{\Phi})\\ &+ 2M(M+1)c_k^2\varepsilon_kf_{kk,4}(\boldsymbol{\Phi}) + 2M(M+1)c_k^2\varepsilon_kf_{kk,2}(\boldsymbol{\Phi})f_{k,3,1}(\boldsymbol{\Phi})\\ &+ 2(M+1)c_k^2\delta\left(f_{k,1,1}(\boldsymbol{\Phi})f_{k,3,1}(\boldsymbol{\Phi}) + f_{kk,5}(\boldsymbol{\Phi})\right) + 2(M+1)c_k^2\delta\varepsilon_kf_{k,1,1}(\boldsymbol{\Phi})f_{kk,2}(\boldsymbol{\Phi})\\ &+ 4(M+1)c_k^2\delta\varepsilon_k\mathrm{Re}\{f_{kk,6}(\boldsymbol{\Phi})\}.\end{aligned} \tag{20}$$

$$\begin{aligned}I_{\mathrm{VR},ki}(\boldsymbol{\Phi}) =& c_kc_i\delta^2\varepsilon_k\varepsilon_iM^2|f_k(\boldsymbol{\Phi})|^2|f_i(\boldsymbol{\Phi})|^2 + c_kc_i\delta^2f_{ki,1,2}(\boldsymbol{\Phi}) + c_kc_i\varepsilon_k\varepsilon_i\Big(Mf_{kk,2}(\boldsymbol{\Phi})f_{ii,2}(\boldsymbol{\Phi})\\ &+ M^2\left|f_{ki,2}(\boldsymbol{\Phi})\right|^2\Big) + c_kc_iM\left(f_{k,3,1}(\boldsymbol{\Phi})f_{i,3,1}(\boldsymbol{\Phi}) + Mf_{ki,3,2}(\boldsymbol{\Phi})\right) + c_kc_i\delta\varepsilon_k\varepsilon_iM\Big(|f_k(\boldsymbol{\Phi})|^2f_{ii,2}(\boldsymbol{\Phi})\\ &+ |f_i(\boldsymbol{\Phi})|^2f_{kk,2}(\boldsymbol{\Phi})\Big) + c_kc_i\delta^2M\Big(\varepsilon_k|f_k(\boldsymbol{\Phi})|^2f_{i,1,1}(\boldsymbol{\Phi}) + \varepsilon_i|f_i(\boldsymbol{\Phi})|^2f_{k,1,1}(\boldsymbol{\Phi})\Big)\\ &+ c_kc_i\delta\varepsilon_k\Big(M|f_k(\boldsymbol{\Phi})|^2f_{i,3,1}(\boldsymbol{\Phi}) + f_{i,1,1}(\boldsymbol{\Phi})f_{kk,2}(\boldsymbol{\Phi})\Big) + c_kc_i\delta\varepsilon_i\Big(M|f_i(\boldsymbol{\Phi})|^2f_{k,3,1}(\boldsymbol{\Phi})\\ &+ f_{k,1,1}(\boldsymbol{\Phi})f_{ii,2}(\boldsymbol{\Phi})\Big) + c_kc_i\delta\left(f_{k,1,1}(\boldsymbol{\Phi})f_{i,3,1}(\boldsymbol{\Phi}) + f_{i,1,1}(\boldsymbol{\Phi})f_{k,3,1}(\boldsymbol{\Phi})\right) + c_kc_i\varepsilon_kM\Big(Mf_{ki,4}(\boldsymbol{\Phi})\\ &+ f_{kk,2}(\boldsymbol{\Phi})f_{i,3,1}(\boldsymbol{\Phi})\Big) + c_kc_i\varepsilon_iM\Big(Mf_{ik,4}(\boldsymbol{\Phi}) + f_{ii,2}(\boldsymbol{\Phi})f_{k,3,1}(\boldsymbol{\Phi})\Big) + \varepsilon_i\mathrm{Re}\big\{f_{ik,6}(\boldsymbol{\Phi})\big\}\\ &+ c_kc_i\delta\varepsilon_k\varepsilon_iM^2\left(f_{ki,7}(\boldsymbol{\Phi})f_{ik,2}(\boldsymbol{\Phi}) + f_{ki,2}(\boldsymbol{\Phi})f_{ik,7}(\boldsymbol{\Phi})\right) + 2c_kc_i\delta M\mathrm{Re}\{f_{ki,5}(\boldsymbol{\Phi})\}\\ &+ 2c_kc_iM\delta\varepsilon_k\mathrm{Re}\big\{f_{ki,6}(\boldsymbol{\Phi})\big\} + 2c_kc_iM\delta\varepsilon_k\mathrm{Re}\big\{f_{ik,6}(\boldsymbol{\Phi})\big\}.\end{aligned} \tag{21}$$

Eqs. (19)–(21) at the top of this page, in which

$$\begin{aligned}
&f_k(\boldsymbol{\Phi}) \triangleq \boldsymbol{a}_N^{\mathrm{H}}\boldsymbol{\Phi}\boldsymbol{D}_k^{1/2}\bar{\boldsymbol{h}}_k,\\
&f_{k,1,1}(\boldsymbol{\Phi}) \triangleq \mathrm{Tr}(\bar{\boldsymbol{H}}_2\boldsymbol{\Phi}\boldsymbol{R}_{\mathrm{VR},k}\boldsymbol{\Phi}^{\mathrm{H}}\bar{\boldsymbol{H}}_2^{\mathrm{H}}),\\
&f_{ki,1,2}(\boldsymbol{\Phi}) \triangleq \mathrm{Tr}\Big((\bar{\boldsymbol{H}}_2\boldsymbol{\Phi}\boldsymbol{R}_{\mathrm{VR},k}\boldsymbol{\Phi}^{\mathrm{H}}\bar{\boldsymbol{H}}_2^{\mathrm{H}})\\
&\qquad\cdot(\bar{\boldsymbol{H}}_2\boldsymbol{\Phi}\boldsymbol{R}_{\mathrm{VR},i}\boldsymbol{\Phi}^{\mathrm{H}}\bar{\boldsymbol{H}}_2^{\mathrm{H}})\Big),\\
&f_{ki,2}(\boldsymbol{\Phi}) \triangleq \bar{\boldsymbol{h}}_k^{\mathrm{H}}\boldsymbol{D}_k^{1/2}\boldsymbol{\Phi}^{\mathrm{H}}\boldsymbol{R}_{\mathrm{ris}}\boldsymbol{\Phi}\boldsymbol{D}_i^{1/2}\bar{\boldsymbol{h}}_i,\\
&f_{k,3,1}(\boldsymbol{\Phi}) \triangleq \mathrm{Tr}\big(\boldsymbol{R}_{\mathrm{ris}}\boldsymbol{\Phi}\boldsymbol{R}_{\mathrm{VR},k}\boldsymbol{\Phi}^{\mathrm{H}}\big),\\
&f_{ki,3,2}(\boldsymbol{\Phi}) \triangleq \mathrm{Tr}\left(\left(\boldsymbol{R}_{\mathrm{ris}}\boldsymbol{\Phi}\boldsymbol{R}_{\mathrm{VR},k}\boldsymbol{\Phi}^{\mathrm{H}}\right)\left(\boldsymbol{R}_{\mathrm{ris}}\boldsymbol{\Phi}\boldsymbol{R}_{\mathrm{VR},i}\boldsymbol{\Phi}^{\mathrm{H}}\right)\right),\\
&f_{ki,4}(\boldsymbol{\Phi}) \triangleq \bar{\boldsymbol{h}}_k^{\mathrm{H}}\boldsymbol{D}_k^{1/2}\boldsymbol{\Phi}^{\mathrm{H}}\boldsymbol{R}_{\mathrm{ris}}\boldsymbol{\Phi}\boldsymbol{R}_{\mathrm{VR},i}\boldsymbol{\Phi}^{\mathrm{H}}\boldsymbol{R}_{\mathrm{ris}}\boldsymbol{\Phi}\boldsymbol{D}_k^{1/2}\bar{\boldsymbol{h}}_k,\\
&f_{ki,5}(\boldsymbol{\Phi}) \triangleq \mathrm{Tr}\big(\bar{\boldsymbol{H}}_2\boldsymbol{\Phi}\boldsymbol{R}_{\mathrm{VR},k}\boldsymbol{\Phi}^{\mathrm{H}}\boldsymbol{R}_{\mathrm{ris}}\boldsymbol{\Phi}\boldsymbol{R}_{\mathrm{VR},i}\boldsymbol{\Phi}^{\mathrm{H}}\bar{\boldsymbol{H}}_2^{\mathrm{H}}\big),\\
&f_{ki,6}(\boldsymbol{\Phi}) \triangleq \bar{\boldsymbol{h}}_k^{\mathrm{H}}\boldsymbol{D}_k^{1/2}\boldsymbol{\Phi}^{\mathrm{H}}\bar{\boldsymbol{H}}_2^{\mathrm{H}}\bar{\boldsymbol{H}}_2\boldsymbol{\Phi}\boldsymbol{R}_{\mathrm{VR},i}\\
&\qquad\cdot\boldsymbol{\Phi}^{\mathrm{H}}\boldsymbol{R}_{\mathrm{ris}}\boldsymbol{\Phi}\boldsymbol{D}_k^{1/2}\bar{\boldsymbol{h}}_k,\\
&f_{ki,7}(\boldsymbol{\Phi}) \triangleq \bar{\boldsymbol{h}}_k^{\mathrm{H}}\boldsymbol{D}_k^{1/2}\boldsymbol{\Phi}^{\mathrm{H}}\boldsymbol{a}_N\boldsymbol{a}_N^{\mathrm{H}}\boldsymbol{\Phi}\boldsymbol{D}_i^{1/2}\bar{\boldsymbol{h}}_i.
\end{aligned} \tag{22}$$

The proof of Theorem 1 is given in the supplementary materials.

Considering the VRs, the derivation process is difficult due to the visibility indicator matrix $\boldsymbol{D}_k$ and the spatial correlation matrices $\boldsymbol{R}_{\mathrm{ris}}$ and $\boldsymbol{R}_{\mathrm{VR},k}$. Nevertheless, expression (18) in Theorem 1 can be calculated quickly without relying on inverse matrices or integrals, resulting in lower computational complexity for evaluating the system performance. Besides, Theorem 1 does not rely on the instantaneous CSI, i.e., $\tilde{\boldsymbol{h}}_k$ and $\tilde{\boldsymbol{H}}_2$, but it depends only on the statistical CSI, i.e., the AoAs and AoDs in $\bar{\boldsymbol{h}}_k$ and $\bar{\boldsymbol{H}}_2$, and the locations of the RIS, the BS, and users, which change slowly and therefore could remain invariant in a long term. As a result, by using the theoretical expression (18) as an objective function for a two-timescale transmission scheme, we can optimize the phase shifts of the XL-RIS determined by only statistical CSI.

On the contrary, by analyzing the derived achievable user rate expression, it can be found that some zero terms exist in the diagonal elements of the visibility indicator matrix $\boldsymbol{D}_k \in \mathbb{C}^{N\times N}$, which

indicates that the RIS elements corresponding to these terms have no contribution to user k. Due to this special property, the dimension of matrix $\boldsymbol{D}_k$ can be further compressed into $N_{k_*}\times N_{k_*}$, assuming that the VR of the k^{th} user contains N_{k*} RIS elements ($N_{k_*}\le N$). Based on Eqs. (1)–(12), we can also reduce the dimension of other matrices, thereby decreasing the computational complexity of the entire system. Specifically, we use $\boldsymbol{a}_{N,k_*}\in\mathbb{C}^{1\times N_{k_*}}$, $\bar{\boldsymbol{h}}_{k_*}\in\mathbb{C}^{N_{k_*}}$, $\bar{\boldsymbol{H}}_{2,k_*}\in\mathbb{C}^{M\times N_{k_*}}$, $\boldsymbol{R}_{\text{VR},k_*}\in\mathbb{C}^{N_{k_*}\times N_{k_*}}$, $\boldsymbol{R}_{\text{ris},k_*,i_*}\in\mathbb{C}^{N_{k_*}\times N_{i_*}}$, and $\boldsymbol{\Phi}_{k_*}\in\mathbb{C}^{N_{k_*}\times N_{k_*}}$ to represent the dimension-reduced matrices of $\boldsymbol{a}_N$, $\bar{\boldsymbol{h}}_k$, $\bar{\boldsymbol{H}}_2$, $\boldsymbol{R}_{\text{VR},k}$, $\boldsymbol{R}_{\text{ris}}$, and $\boldsymbol{\Phi}$, respectively. The detailed results are given as follows:

$$\begin{cases}[\boldsymbol{a}_{N,k_*}]_q=[\boldsymbol{a}_N]_{[\tau_k]_q},\\ [\bar{\boldsymbol{h}}_{k_*}]_q=[\bar{\boldsymbol{h}}_k]_{[\tau_k]_q},\\ [\bar{\boldsymbol{H}}_{2,k_*}]_{(:,q)}=[\bar{\boldsymbol{H}}_2]_{(:,[\tau_k]_q)},\\ [\boldsymbol{R}_{\text{VR},k_*}]_{(l,q)}=[\boldsymbol{R}_{\text{VR},k}]_{([\tau_k]_l,[\tau_k]_q)},\\ [\boldsymbol{R}_{\text{ris},i_*,k_*}]_{(l,q)}=[\boldsymbol{R}_{\text{ris}}]_{([\tau_i]_l,[\tau_k]_q)},\\ [\boldsymbol{\Phi}_{k_*}]_{(:,q)}=[\boldsymbol{\Phi}]_{(:,[\tau_k]_q)},\end{cases}\tag{23}$$

where $q\in\{1,2,\dots,N_{k_*}\}$ and $l\in\{1,2,\dots,N_{i_*}\}$. Besides, $[\tau_k]_q$ presents the q^{th} element of set τ_k. As a result, the expressions in Eq. (22) can be rewritten as follows:

$$\begin{aligned}
&f_{k_*}(\boldsymbol{\Phi})\triangleq\boldsymbol{a}_{N,k_*}^{\text{H}}\boldsymbol{\Phi}_{k_*}\bar{\boldsymbol{h}}_{k_*},\\
&f_{k_*,1,1}(\boldsymbol{\Phi})\triangleq\text{Tr}\big(\bar{\boldsymbol{H}}_{2,k_*}\boldsymbol{\Phi}_{k_*}\boldsymbol{R}_{\text{VR},k_*}\boldsymbol{\Phi}_{k_*}^{\text{H}}\bar{\boldsymbol{H}}_{2,k_*}^{\text{H}}\big),\\
&f_{k_*,i_*,1,2}(\boldsymbol{\Phi})\triangleq\text{Tr}\Big(\big(\bar{\boldsymbol{H}}_{2,k_*}\boldsymbol{\Phi}_{k_*}\boldsymbol{R}_{\text{VR},k_*}\boldsymbol{\Phi}_{k_*}^{\text{H}}\bar{\boldsymbol{H}}_{2,k_*}^{\text{H}}\big)\\
&\qquad\cdot\big(\bar{\boldsymbol{H}}_{2,i_*}\boldsymbol{\Phi}_{i_*}\boldsymbol{R}_{\text{VR},i_*}\boldsymbol{\Phi}_{i_*}^{\text{H}}\bar{\boldsymbol{H}}_{2,i_*}^{\text{H}}\big)\Big),\\
&f_{k_*,i_*,2}(\boldsymbol{\Phi})\triangleq\bar{\boldsymbol{h}}_{k_*}^{\text{H}}\boldsymbol{\Phi}_{k_*}^{\text{H}}\boldsymbol{R}_{\text{ris},k_*,i_*}\boldsymbol{\Phi}_{i_*}\bar{\boldsymbol{h}}_{i_*},\\
&f_{k_*,3,1}(\boldsymbol{\Phi})\triangleq\text{Tr}(\boldsymbol{R}_{\text{ris},k_*,k_*}\boldsymbol{\Phi}_{k_*}\boldsymbol{R}_{\text{VR},k_*}\boldsymbol{\Phi}_{k_*}^{\text{H}}),\\
&f_{k_*,i_*,3,2}(\boldsymbol{\Phi})\triangleq\text{Tr}\Big(\big(\boldsymbol{R}_{\text{ris},i_*,k_*}\boldsymbol{\Phi}_{k_*}\boldsymbol{R}_{\text{VR},k_*}\boldsymbol{\Phi}_{k_*}^{\text{H}}\big)\\
&\qquad\cdot\big(\boldsymbol{R}_{\text{ris},k_*,i_*}\boldsymbol{\Phi}_{i_*}\boldsymbol{R}_{\text{VR},i_*}\boldsymbol{\Phi}_{i_*}^{\text{H}}\big)\Big),\\
&f_{k_*,i_*,4}(\boldsymbol{\Phi})\triangleq\bar{\boldsymbol{h}}_{k_*}^{\text{H}}\boldsymbol{\Phi}_{k_*}^{\text{H}}\boldsymbol{R}_{\text{ris},k_*,i_*}\boldsymbol{\Phi}_{i_*}\boldsymbol{R}_{\text{VR},i_*}\boldsymbol{\Phi}_{i_*}^{\text{H}}\\
&\qquad\cdot\boldsymbol{R}_{\text{ris},i_*,k_*}\boldsymbol{\Phi}_{k_*}\bar{\boldsymbol{h}}_{k_*},\\
&f_{k_*,i_*,5}(\boldsymbol{\Phi})\triangleq\text{Tr}\left(\bar{\boldsymbol{H}}_{2,k_*}\boldsymbol{\Phi}_{k_*}\boldsymbol{R}_{\text{VR},k_*}\boldsymbol{\Phi}_{k_*}^{\text{H}}\boldsymbol{R}_{\text{ris},k_*,i_*}\right.\\
&\qquad\left.\cdot\boldsymbol{\Phi}_{i_*}\boldsymbol{R}_{\text{VR},i_*}\boldsymbol{\Phi}_{i_*}^{\text{H}}\bar{\boldsymbol{H}}_{2,i_*}^{\text{H}}\right),\\
&f_{k_*,i_*,6}(\boldsymbol{\Phi})\triangleq\bar{\boldsymbol{h}}_{k_*}^{\text{H}}\boldsymbol{\Phi}_{k_*}^{\text{H}}\bar{\boldsymbol{H}}_{2,k_*}^{\text{H}}\bar{\boldsymbol{H}}_{2,i_*}\boldsymbol{\Phi}_{i_*}\boldsymbol{R}_{\text{VR},i_*}\boldsymbol{\Phi}_{i_*}^{\text{H}}\\
&\qquad\cdot\boldsymbol{R}_{\text{ris},i_*,k_*}\boldsymbol{\Phi}_{k_*}\bar{\boldsymbol{h}}_{k_*},\\
&f_{k_*,i_*,7}(\boldsymbol{\Phi})\triangleq\bar{\boldsymbol{h}}_{k_*}^{\text{H}}\boldsymbol{\Phi}_{k_*}^{\text{H}}\boldsymbol{a}_{N,k_*}\boldsymbol{a}_{N,i_*}^{\text{H}}\boldsymbol{\Phi}_{i_*}\bar{\boldsymbol{h}}_{i_*}.
\end{aligned}\tag{24}$$

Due to the lower dimensionality of the participating matrices, the computations in Eq. (24) are comparatively simpler than those in Eq. (22). Specifically, the complexity reduction is attributed to the VR where a certain user k can observe only a subset of RIS elements ($N_{k_*}\le N$). By substituting Eq. (24) into Eqs. (18)–(21), the achievable user rate can be conveniently computed.

4 RIS phase shift design

In this section, we optimize the phase shifts of the RIS to maximize the achievable rate derived from expression (18). In a MU scenario, it is necessary to ensure fairness among different users. Therefore, we consider the minimum achievable user rate maximization problem. Specifically, this problem can be formulated as follows:

$$\max_{\boldsymbol{\Phi}}\ \min_{k}\ \text{RATE}_{\text{VR},k}\ \text{ s.t. }\left|[\boldsymbol{\Phi}]_{n,n}\right|=1,\ \forall n,\tag{25}$$

where $\text{RATE}_{\text{VR},k}$ is the achievable user rate obtained from expression (18).

From Eqs. (18)–(22), it can be observed that the objective function of the optimization problem becomes more intricate when spatial correlation and VRs are present. Besides, when N is large, the dimension of matrices in calculation can be extremely high, which leads to low algorithm efficiency. Fortunately, we have investigated the beneficial effects of VRs in Section 3 and found that they can decrease the computational complexity of the entire system. Furthermore, we need a new algorithm to better address the considered minimum user rate maximization problem.

We propose a gradient-based algorithm with respect to real variable θ_n instead of complex variable $\text{e}^{\text{j}\theta_n}$, where θ_n is the phase of the n^{th} RIS element. Since the objective function in Problem (25) contains a non-differentiable minimum function, to conduct the gradient algorithm, we first employ the Lagrangian duality and Jaynes' maximum entropy principle (Jaynes, 1957) to approximate the objective function in Problem (25) as follows:

$$\begin{aligned}&\min_{k}\ \text{RATE}_{\text{VR},k}(\boldsymbol{\theta})\\ \approx&-\frac{1}{\mu}\ln\left\{\sum_{k=1}^{K}\exp\left[-\mu\text{RATE}_{\text{VR},k}(\boldsymbol{\theta})\right]\right\}\triangleq f_{\text{VR}}(\boldsymbol{\theta}),\end{aligned}\tag{26}$$

where $\boldsymbol{\theta}=[\theta_1,\theta_2,...,\theta_N]^{\mathrm{T}}$ is the new optimization variable and μ is a constant controlling the approximation accuracy, which can be proved that the approximation error is less than $\frac{\ln K}{\mu}$ (Li XS, 1992). It also can be shown that $f_{\mathrm{VR}}(\boldsymbol{\theta})$ will approach $\mathrm{RATE}_{\mathrm{VR},k}$ as the parameter μ tends to infinity. Therefore, Problem (25) can be rewritten as follows:

$$\begin{aligned}&\max_{\boldsymbol{\Phi}}\ f_{\mathrm{VR}}(\boldsymbol{\theta})\\&\text{s.t. }\theta_n\in[0,2\pi),\ \forall n.\end{aligned}\tag{27}$$

Due to the periodicity of the objective function $f_{\mathrm{VR}}(\boldsymbol{\theta})$ relative to $\boldsymbol{\theta}$, the constraint in Problem (27) can be ignored, which effectively tackles the unit-modulus constraint in Problem (25). To update variable $\boldsymbol{\theta}$, the gradient of $f_{\mathrm{VR}}(\boldsymbol{\theta})$ needs to be calculated as follows:

$$\frac{\partial f_{\mathrm{VR}}(\boldsymbol{\theta})}{\partial\boldsymbol{\theta}}=\frac{\sum\limits_{k=1}^{K}\left\{\frac{\exp[-\mu\mathrm{RATE}_{\mathrm{VR},k}(\boldsymbol{\theta})]}{1+\mathrm{SINR}_{\mathrm{VR},k}(\boldsymbol{\theta})}\frac{\partial\,\mathrm{SINR}_{\mathrm{VR},k}(\boldsymbol{\theta})}{\partial\boldsymbol{\theta}}\right\}}{(\ln 2)\left\{\sum\limits_{k=1}^{K}\exp[-\mu\mathrm{RATE}_{\mathrm{VR},k}(\boldsymbol{\theta})]\right\}},\tag{28}$$

where

$$\begin{aligned}\frac{\partial\,\mathrm{SINR}_{\mathrm{VR},k}(\boldsymbol{\theta})}{\partial\boldsymbol{\theta}}=&\frac{p\dfrac{\partial E_{\mathrm{VR},k}^{\mathrm{signal}}}{\partial\boldsymbol{\theta}}}{p\sum\limits_{i=1,i\neq k}^{K}I_{\mathrm{VR},ki}+\sigma^2E_{\mathrm{VR},k}^{\mathrm{noise}}}\\&-pE_{\mathrm{VR},k}^{\mathrm{signal}}\frac{p\sum\limits_{i=1,i\neq k}^{K}\dfrac{\partial I_{\mathrm{VR},ki}}{\partial\boldsymbol{\theta}}+\sigma^2\dfrac{\partial E_{\mathrm{VR},k}^{\mathrm{noise}}}{\partial\boldsymbol{\theta}}}{\left(p\sum\limits_{i=1,i\neq k}^{K}I_{\mathrm{VR},ki}+\sigma^2E_{\mathrm{VR},k}^{\mathrm{noise}}\right)^2}.\end{aligned}\tag{29}$$

According to Eqs. (28) and (29), the gradient of $f_{\mathrm{VR}}(\boldsymbol{\theta})$ can be obtained by calculating the gradients of $E_{\mathrm{VR},k}^{\mathrm{noise}}(\boldsymbol{\Phi})$, $E_{\mathrm{VR},k}^{\mathrm{signal}}(\boldsymbol{\Phi})$, and $\sum_{i=1,i\neq k}^{K}I_{\mathrm{VR},ki}(\boldsymbol{\Phi})$. By using the conclusion of Lemma 1 in Zhi et al. (2023), we define the following:

$$\begin{aligned}\boldsymbol{f}_a(\boldsymbol{A},\boldsymbol{B})\triangleq&\frac{\partial\,\mathrm{Tr}\left(\boldsymbol{A}\boldsymbol{\Phi}\boldsymbol{B}\boldsymbol{\Phi}^{\mathrm{H}}\right)}{\partial\boldsymbol{\theta}}\\=&\mathrm{j}\boldsymbol{\Phi}^{\mathrm{T}}(\boldsymbol{A}^{\mathrm{T}}\odot\boldsymbol{B})\boldsymbol{c}^*-\mathrm{j}\boldsymbol{\Phi}^{\mathrm{H}}(\boldsymbol{A}\odot\boldsymbol{B}^{\mathrm{T}})\boldsymbol{c},\end{aligned}\tag{30}$$

where $\boldsymbol{A}$ and $\boldsymbol{B}$ are deterministic matrices, $\boldsymbol{c}=[\mathrm{e}^{\mathrm{j}\theta_1},\mathrm{e}^{\mathrm{j}\theta_2},\ldots,\mathrm{e}^{\mathrm{j}\theta_N}]^{\mathrm{T}}$, and $\boldsymbol{c}^*$ is the conjugate of $\boldsymbol{c}$. Then, the gradients of the auxiliary functions in Eq. (22) can be calculated as follows:

$$\begin{aligned}&f'_k(\boldsymbol{\theta})\triangleq\boldsymbol{f}_a(\boldsymbol{a}_N\boldsymbol{a}_N^{\mathrm{H}},\boldsymbol{D}_k^{1/2}\bar{\boldsymbol{h}}_k\bar{\boldsymbol{h}}_k^{\mathrm{H}}\boldsymbol{D}_k^{1/2}),\\&f'_{k,1,1}(\boldsymbol{\theta})\triangleq\boldsymbol{f}_a(\bar{\boldsymbol{H}}_2^{\mathrm{H}}\bar{\boldsymbol{H}}_2,\boldsymbol{R}_{\mathrm{VR},k}),\\&f'_{ki,1,2}(\boldsymbol{\theta})\triangleq\boldsymbol{f}_a(\bar{\boldsymbol{H}}_2^{\mathrm{H}}\bar{\boldsymbol{H}}_2\boldsymbol{\Phi}\boldsymbol{R}_{\mathrm{VR},i}\boldsymbol{\Phi}^{\mathrm{H}}\bar{\boldsymbol{H}}_2^{\mathrm{H}}\bar{\boldsymbol{H}}_2,\boldsymbol{R}_{\mathrm{VR},k})\\&\qquad+\boldsymbol{f}_a(\bar{\boldsymbol{H}}_2^{\mathrm{H}}\bar{\boldsymbol{H}}_2\boldsymbol{\Phi}\boldsymbol{R}_{\mathrm{VR},k}\boldsymbol{\Phi}^{\mathrm{H}}\bar{\boldsymbol{H}}_2^{\mathrm{H}}\bar{\boldsymbol{H}}_2,\boldsymbol{R}_{\mathrm{VR},i}),\\&f'_{ki,2}(\boldsymbol{\theta})\triangleq\boldsymbol{f}_a(\boldsymbol{R}_{\mathrm{ris}},\boldsymbol{D}_i^{1/2}\bar{\boldsymbol{h}}_i\bar{\boldsymbol{h}}_k^{\mathrm{H}}\boldsymbol{D}_k^{1/2}),\\&f'_{k,3,1}(\boldsymbol{\theta})\triangleq\boldsymbol{f}_a(\boldsymbol{R}_{\mathrm{ris}},\boldsymbol{R}_{\mathrm{VR},k}),\\&f'_{ki,3,2}(\boldsymbol{\theta})\triangleq\boldsymbol{f}_a\big(\boldsymbol{R}_{\mathrm{ris}}\boldsymbol{\Phi}\boldsymbol{R}_{\mathrm{VR},i}\boldsymbol{\Phi}^{\mathrm{H}}\boldsymbol{R}_{\mathrm{ris}},\boldsymbol{R}_{\mathrm{VR},k}\big)\\&\qquad+\boldsymbol{f}_a(\boldsymbol{R}_{\mathrm{ris}}\boldsymbol{\Phi}\boldsymbol{R}_{\mathrm{VR},k}\boldsymbol{\Phi}^{\mathrm{H}}\boldsymbol{R}_{\mathrm{ris}},\boldsymbol{R}_{\mathrm{VR},i}),\\&f'_{ki,4}(\boldsymbol{\theta})\triangleq\boldsymbol{f}_a\big(\boldsymbol{R}_{\mathrm{ris}}\boldsymbol{\Phi}\boldsymbol{D}_k^{1/2}\bar{\boldsymbol{h}}_k\bar{\boldsymbol{h}}_k^{\mathrm{H}}\boldsymbol{D}_k^{1/2}\boldsymbol{\Phi}^{\mathrm{H}}\boldsymbol{R}_{\mathrm{ris}},\boldsymbol{R}_{\mathrm{VR},i}\big)\\&\qquad+\boldsymbol{f}_a(\boldsymbol{R}_{\mathrm{ris}}\boldsymbol{\Phi}\boldsymbol{R}_{\mathrm{VR},i}\boldsymbol{\Phi}^{\mathrm{H}}\boldsymbol{R}_{\mathrm{ris}},\boldsymbol{D}_k^{1/2}\bar{\boldsymbol{h}}_k\bar{\boldsymbol{h}}_k^{\mathrm{H}}\boldsymbol{D}_k^{1/2}),\\&f'_{ki,5}(\boldsymbol{\theta})\triangleq\boldsymbol{f}_a(\bar{\boldsymbol{H}}_2^{\mathrm{H}}\bar{\boldsymbol{H}}_2\boldsymbol{\Phi}\boldsymbol{R}_{\mathrm{VR},k}\boldsymbol{\Phi}^{\mathrm{H}}\boldsymbol{R}_{\mathrm{ris}},\boldsymbol{R}_{\mathrm{VR},i})\\&\qquad+\boldsymbol{f}_a(\boldsymbol{R}_{\mathrm{ris}}\boldsymbol{\Phi}\boldsymbol{R}_{\mathrm{VR},i}\boldsymbol{\Phi}^{\mathrm{H}}\bar{\boldsymbol{H}}_2^{\mathrm{H}}\bar{\boldsymbol{H}}_2,\boldsymbol{R}_{\mathrm{VR},k}),\\&f'_{ki,6}(\boldsymbol{\theta})\triangleq\boldsymbol{f}_a(\boldsymbol{R}_{\mathrm{ris}}\boldsymbol{\Phi}\boldsymbol{D}_k^{1/2}\bar{\boldsymbol{h}}_k\bar{\boldsymbol{h}}_k^{\mathrm{H}}\boldsymbol{D}_k^{1/2}\boldsymbol{\Phi}^{\mathrm{H}}\bar{\boldsymbol{H}}_2^{\mathrm{H}}\bar{\boldsymbol{H}}_2,\boldsymbol{R}_{\mathrm{VR},i})\\&\qquad+\boldsymbol{f}_a(\bar{\boldsymbol{H}}_2^{\mathrm{H}}\bar{\boldsymbol{H}}_2\boldsymbol{\Phi}\boldsymbol{R}_{\mathrm{VR},i}\boldsymbol{\Phi}^{\mathrm{H}}\boldsymbol{R}_{\mathrm{ris}},\boldsymbol{D}_k^{1/2}\bar{\boldsymbol{h}}_k\bar{\boldsymbol{h}}_k^{\mathrm{H}}\boldsymbol{D}_k^{1/2}),\\&f^*_{ik,6}(\boldsymbol{\theta})\triangleq\boldsymbol{f}_a(\bar{\boldsymbol{H}}_2^{\mathrm{H}}\bar{\boldsymbol{H}}_2\boldsymbol{\Phi}\boldsymbol{D}_k^{1/2}\bar{\boldsymbol{h}}_k\bar{\boldsymbol{h}}_k^{\mathrm{H}}\boldsymbol{D}_k^{1/2}\boldsymbol{\Phi}^{\mathrm{H}}\boldsymbol{R}_{\mathrm{ris}},\boldsymbol{R}_{\mathrm{VR},i})\\&\quad+\boldsymbol{f}_a\left(\boldsymbol{R}_{\mathrm{ris}}\boldsymbol{\Phi}\boldsymbol{R}_{\mathrm{VR},i}\boldsymbol{\Phi}^{\mathrm{H}}\bar{\boldsymbol{H}}_2^{\mathrm{H}}\bar{\boldsymbol{H}}_2,\boldsymbol{D}_k^{1/2}\bar{\boldsymbol{h}}_k\bar{\boldsymbol{h}}_k^{\mathrm{H}}\boldsymbol{D}_k^{1/2}\right),\\&f'_{ki,7}(\boldsymbol{\theta})\triangleq\boldsymbol{f}_a\big(\boldsymbol{a}_N\boldsymbol{a}_N^{\mathrm{H}},\boldsymbol{D}_i^{1/2}\bar{\boldsymbol{h}}_i\bar{\boldsymbol{h}}_k^{\mathrm{H}}\boldsymbol{D}_k^{1/2}\big).\end{aligned}\tag{31}$$

Then, $\frac{\partial E_{\mathrm{VR},k}^{\mathrm{noise}}}{\partial\boldsymbol{\theta}}$, $\frac{\partial E_{\mathrm{VR},k}^{\mathrm{signal}}}{\partial\boldsymbol{\theta}}$, and $\frac{\partial I_{\mathrm{VR},ki}}{\partial\boldsymbol{\theta}}$ can be derived using the above results and the chain rule. The results are given in Eqs. (32)–(34) at the top of the next page.

The complete process for solving Problem (27) is provided in Algorithm 1. To improve the convergence performance, the Nesterov accelerated gradient method as shown in steps 6 and 7 is used in the algorithm.

In Algorithm 1, $\boldsymbol{\theta}^*$ is the optimized solution, from which the RIS phase shift matrix $\boldsymbol{\Phi}$ can be calculated. After obtaining $\boldsymbol{\Phi}$, it can be applied to the original Problem (25) to obtain the maximum value of the minimum achievable rate. At the same time, the results show that the complexity of Eq. (28) is $\mathcal{O}(MN^2+M^2N+N^3)$, which depends only on the fundamental system parameters. Therefore, relying on simple matrix operations, the two-timescale transmission scheme based on the gradient algorithm can significantly reduce the computational complexity.

$$\frac{\partial E_{\mathrm{VR},k}^{\mathrm{noise}}}{\partial \boldsymbol{\theta}} = c_k \left[M\delta\varepsilon_k f_k'(\boldsymbol{\theta}) + \delta f_{k,1,1}'(\boldsymbol{\theta}) + \varepsilon_k f_{kk,2}'(\boldsymbol{\theta}) M + f_{k,3,1}'(\boldsymbol{\theta}) M \right]. \tag{32}$$

$$\begin{aligned}
\frac{\partial E_{\mathrm{VR},k}^{\mathrm{signal}}}{\partial \boldsymbol{\theta}} =& M^2 (c_k\delta\varepsilon_k)^2 |f_k(\boldsymbol{\Phi})|^2 f_k'(\boldsymbol{\theta}) + (c_k\delta)^2 \left(f_{kk,1,2}'(\boldsymbol{\theta}) + 2 f_{k,1,1}(\boldsymbol{\Phi}) f_{k,1,1}'(\boldsymbol{\theta}) \right) \\
&+ 2(c_k\varepsilon_k)^2 M(M+1) f_{kk,2}(\boldsymbol{\Phi}) f_{kk,2}'(\boldsymbol{\theta}) + c_k^2 M(M+1) \left(f_{kk,3,2}'(\boldsymbol{\theta}) + 2 f_{k,3,1}'(\boldsymbol{\theta}) f_{k,3,1}(\boldsymbol{\Phi}) \right) \\
&+ 4M(c_k\delta)^2 \varepsilon_k \left(f_{k,1,1}'(\boldsymbol{\theta}) |f_k(\boldsymbol{\Phi})|^2 + f_{k,1,1}(\boldsymbol{\Phi}) f_k'(\boldsymbol{\theta}) \right) + 2M(M+1)(c_k\varepsilon_k)^2 \delta f_{kk,2}'(\boldsymbol{\theta}) |f_k(\boldsymbol{\Phi})|^2 \\
&+ 2M(M+1)(c_k\varepsilon_k)^2 \delta f_{kk,2}(\boldsymbol{\Phi}) f_k'(\boldsymbol{\theta}) + 2M(M+1) c_k^2 \delta\varepsilon_k f_{k,3,1}'(\boldsymbol{\theta}) |f_k(\boldsymbol{\Phi})|^2 \\
&+ 2M(M+1) c_k^2 \delta\varepsilon_k f_{k,3,1}(\boldsymbol{\Phi}) f_k'(\boldsymbol{\theta}) + 2(M+1) c_k^2 \delta\varepsilon_k f_{kk,2}'(\boldsymbol{\theta}) f_{k,1,1}(\boldsymbol{\Phi}) \\
&+ 2(M+1) c_k^2 \delta\varepsilon_k f_{kk,2}(\boldsymbol{\Phi}) f_{k,1,1}'(\boldsymbol{\theta}) + 2(M+1) c_k^2 \delta f_{k,3,1}'(\boldsymbol{\theta}) f_{k,1,1}(\boldsymbol{\Phi}) \\
&+ 2(M+1) c_k^2 \delta \left(f_{k,3,1}(\boldsymbol{\Phi}) f_{k,1,1}'(\boldsymbol{\theta}) + f_{kk,5}'(\boldsymbol{\theta}) \right) + 2M(M+1) c_k^2 \varepsilon_k f_{k,3,1}'(\boldsymbol{\theta}) f_{kk,2}(\boldsymbol{\Phi}) \\
&+ 2M(M+1) c_k^2 \varepsilon_k \left(f_{k,3,1}(\boldsymbol{\Phi}) f_{kk,2}'(\boldsymbol{\theta}) + f_{kk,4}'(\boldsymbol{\theta}) \right) + 2(M+1) c_k^2 \delta\varepsilon_k \left(f_{kk,6}'(\boldsymbol{\theta}) + f_{kk,6}^*(\boldsymbol{\theta}) \right).
\end{aligned} \tag{33}$$

$$\begin{aligned}
\frac{\partial I_{\mathrm{VR},ki}}{\partial \boldsymbol{\theta}} =& c_k c_i \delta^2 \varepsilon_k \varepsilon_i M^2 \left(f_k'(\boldsymbol{\theta}) |f_i(\boldsymbol{\Phi})|^2 + |f_k(\boldsymbol{\Phi})|^2 f_i'(\boldsymbol{\theta}) \right) + c_k c_i \delta^2 f_{ki,1,2}'(\boldsymbol{\theta}) \\
&+ c_k c_i \varepsilon_k \varepsilon_i M \left(f_{kk,2}(\boldsymbol{\Phi}) f_{ii,2}'(\boldsymbol{\theta}) + f_{kk,2}'(\boldsymbol{\theta}) f_{ii,2}(\boldsymbol{\Phi}) \right) + c_k c_i \varepsilon_k \varepsilon_i M^2 \big(f_{ik,2}(\boldsymbol{\Phi}) f_{ki,2}'(\boldsymbol{\theta}) \\
&+ f_{ki,2}(\boldsymbol{\Phi}) f_{ik,2}'(\boldsymbol{\theta}) \big) + c_k c_i M \left(f_{k,3,1}(\boldsymbol{\Phi}) f_{i,3,1}'(\boldsymbol{\theta}) + f_{k,3,1}'(\boldsymbol{\theta}) f_{i,3,1}(\boldsymbol{\Phi}) \right) \\
&+ c_k c_i \delta\varepsilon_k \varepsilon_i M \left(|f_k(\boldsymbol{\Phi})|^2 f_{ii,2}'(\boldsymbol{\theta}) + f_k'(\boldsymbol{\theta}) f_{ii,2}(\boldsymbol{\Phi}) \right) + c_k c_i \delta\varepsilon_k \varepsilon_i M \left(|f_i(\boldsymbol{\Phi})|^2 f_{kk,2}'(\boldsymbol{\theta}) + f_i'(\boldsymbol{\theta}) f_{kk,2}(\boldsymbol{\Phi}) \right) \\
&+ c_k c_i \delta^2 \varepsilon_k M \left(|f_k(\boldsymbol{\Phi})|^2 f_{i,1,1}'(\boldsymbol{\theta}) + f_k'(\boldsymbol{\theta}) f_{i,1,1}(\boldsymbol{\Phi}) \right) + c_k c_i \delta^2 \varepsilon_i M \left(|f_i(\boldsymbol{\Phi})|^2 f_{k,1,1}'(\boldsymbol{\theta}) + f_i'(\boldsymbol{\theta}) f_{k,1,1}(\boldsymbol{\Phi}) \right) \\
&+ c_k c_i \delta\varepsilon_k M \left(|f_k(\boldsymbol{\Phi})|^2 f_{i,3,1}'(\boldsymbol{\theta}) + f_k'(\boldsymbol{\theta}) f_{i,3,1}(\boldsymbol{\Phi}) \right) + c_k c_i \delta\varepsilon_k \left(f_{i,1,1}(\boldsymbol{\Phi}) f_{kk,2}'(\boldsymbol{\theta}) + f_{i,1,1}'(\boldsymbol{\theta}) f_{kk,2}(\boldsymbol{\Phi}) \right) \\
&+ c_k c_i \delta\varepsilon_i M \left(|f_i(\boldsymbol{\Phi})|^2 f_{k,3,1}'(\boldsymbol{\theta}) + f_i'(\boldsymbol{\theta}) f_{k,3,1}(\boldsymbol{\Phi}) \right) + c_k c_i \delta\varepsilon_i \left(f_{ii,2}'(\boldsymbol{\theta}) f_{k,1,1}(\boldsymbol{\Phi}) + f_{ii,2}(\boldsymbol{\Phi}) f_{k,1,1}'(\boldsymbol{\theta}) \right) \\
&+ c_k c_i \delta \left(f_{i,3,1}'(\boldsymbol{\theta}) f_{k,1,1}(\boldsymbol{\Phi}) + f_{i,3,1}(\boldsymbol{\Phi}) f_{k,1,1}'(\boldsymbol{\theta}) \right) + c_k c_i \delta \left(f_{i,1,1}(\boldsymbol{\Phi}) f_{k,3,1}'(\boldsymbol{\theta}) + f_{i,1,1}'(\boldsymbol{\theta}) f_{k,3,1}(\boldsymbol{\Phi}) \right) \\
&+ c_k c_i \varepsilon_k M \left(f_{i,3,1}'(\boldsymbol{\theta}) f_{kk,2}(\boldsymbol{\Phi}) + f_{i,3,1}(\boldsymbol{\Phi}) f_{kk,2}'(\boldsymbol{\theta}) \right) + c_k c_i \varepsilon_i M \left(f_{k,3,1}'(\boldsymbol{\theta}) f_{ii,2}(\boldsymbol{\Phi}) + f_{k,3,1}(\boldsymbol{\Phi}) f_{ii,2}'(\boldsymbol{\theta}) \right) \\
&+ c_k c_i \delta\varepsilon_k \varepsilon_i M^2 \left(f_{ik,2}'(\boldsymbol{\theta}) f_{ki,7}(\boldsymbol{\Phi}) + f_{ik,2}(\boldsymbol{\Phi}) f_{ki,7}'(\boldsymbol{\theta}) \right) + c_k c_i \varepsilon_i M^2 f_{ik,4}'(\boldsymbol{\theta}) \\
&+ c_k c_i \delta\varepsilon_k \varepsilon_i M^2 \left(f_{ki,2}'(\boldsymbol{\theta}) f_{ik,7}(\boldsymbol{\Phi}) + f_{ki,2}(\boldsymbol{\Phi}) f_{ik,7}'(\boldsymbol{\theta}) \right) + c_k c_i \delta M \left(f_{ki,5}'(\boldsymbol{\theta}) + f_{ik,5}'(\boldsymbol{\theta}) \right) \\
&+ c_k c_i M^2 f_{ki,3,2}'(\boldsymbol{\theta}) + c_k c_i \varepsilon_k M^2 f_{ki,4}'(\boldsymbol{\theta}) + 2 c_k c_i \delta\varepsilon_k M \left(f_{ki,6}'(\boldsymbol{\theta}) + f_{ki,6}^*(\boldsymbol{\theta}) \right) \\
&+ 2 c_k c_i \delta\varepsilon_i M \left(f_{ik,6}'(\boldsymbol{\theta}) + f_{ik,6}^*(\boldsymbol{\theta}) \right).
\end{aligned} \tag{34}$$

5 Simulations and results

In this section, we evaluate the performance of XL-RIS-aided massive MIMO systems and validate the correctness of our analysis. We also illustrate the impact of key parameters. First, a typical XL-RIS-aided scenario is considered where the XL-RIS is deployed near some cell-edge users. We assume that $K = 4$ users are evenly located on a semicircle centered at the XL-RIS with a radius of $d_{\mathrm{UI}} = 15$ m. The distance between the BS and the XL-RIS is $d_{\mathrm{IB}} = 800$ m. All AoAs and AoDs of BS, XL-RIS, and users are randomly generated from $[0, 2\pi)$, and these parameters will be fixed as known after initial generation. Besides, we set the distance-dependent large-scale path-loss factors equal to $\alpha_k = 10^{-3} d_{\mathrm{UI}}^{\alpha_{k,\mathrm{UR}}}$ $(\forall k)$ and $\beta = 10^{-3} d_{\mathrm{IB}}^{\beta_{\mathrm{RB}}}$, and the path-loss exponents are $\alpha_{k,\mathrm{UR}} = 2$ $(\forall k)$ and $\beta_{\mathrm{RB}} = 2.5$. Due to the dual consideration of time cost and accuracy, we set the approximation factor μ to 100. Considering the impact of VRs, we assume that each user can only see the XL-RIS elements within a certain region of the entire UPA model. To simulate the complexity of the actual environment, we randomly set the size and location of the VRs for different users. The other simulation parameters are presented in Table 1.

Algorithm 1 Gradient algorithm

Randomly initialize $\boldsymbol{\theta}_0$ and set $i=0, e_0=1, \boldsymbol{x}_{-1}=\boldsymbol{\theta}_0$
while 1 **do**
  Calculate $f'_{\mathrm{VR}}(\boldsymbol{\theta}_i)$
  Obtain the step size κ_i based on the backtracking line search
  $\boldsymbol{x}_i=\boldsymbol{\theta}_i+\kappa_i f'_{\mathrm{VR}}(\boldsymbol{\theta}_i)$
  $e_{i+1}=(1+\sqrt{4e_i^2+1})/2$
  $\boldsymbol{\theta}_{i+1}=\boldsymbol{x}_i+(e_i-1)(\boldsymbol{x}_i-\boldsymbol{x}_{i-1})/e_{i+1}$
  if $f_{\mathrm{VR}}(\boldsymbol{\theta}_{i+1})-f_{\mathrm{VR}}(\boldsymbol{\theta}_i)<10^{-4}$ **then**
    $\boldsymbol{\theta}^*=\boldsymbol{\theta}_{i+1}$, break
  end if
  $i=i+1$
end while

Table 1 Simulation parameters

Parameter	Value
Number of BS antennas	$M=64$
RIS element spacing	$d_{\mathrm{ris}}=\lambda/2$
Number of RIS elements	$N=200$
Antenna spacing	$d_{\mathrm{bs}}=\lambda/2$
Rician factors	$\delta=1,\ \varepsilon_k=10,\ \forall k$
Transmit power	$p=30$ dBm

BS: base station; RIS: reconfigurable intelligent surface

Figs. 3 and 4 show the relationship between M or N and the minimum user rate when considering the VR of RIS, respectively. The comparison between theoretical and simulation results demonstrates that the obtained approximate achievable rate in expression (18) is in good agreement with the Monte–Carlo simulation results, confirming the accuracy of the mathematical derivations. In addition, as shown in Fig. 3, it can be confirmed that as the number of antennas M increases, the minimum user rate gradually increases. Although the rate eventually converges to a theoretical limit, which is due to the inter-user interference, it can be significantly improved by increasing the number of N. On the contrary, deploying RIS results in promising throughput with a moderate number of antennas, which reduces power consumption and hardware costs. For instance, 60 antennas with 400 RIS elements could perform better than 120 antennas with 200 RIS elements, thanks to the RIS passive beamforming gain.

In Figs. 3 and 4, "partial visibility" indicates that each user can only see partial non-overlapping RIS elements, while "full visibility" indicates that each user can see all RIS elements, i.e., a special case without spatial non-stationary. It can be observed that the minimum user rate is relatively low when

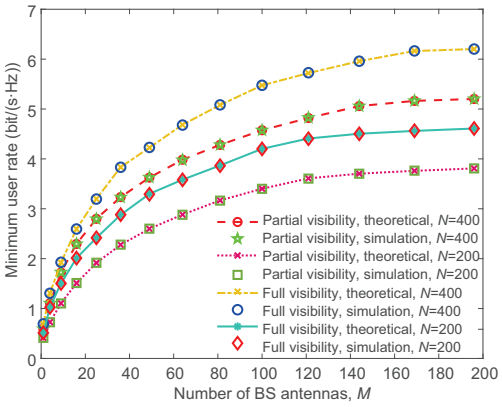

Fig. 3 Minimum user rate versus number of BS antennas (BS: base station)

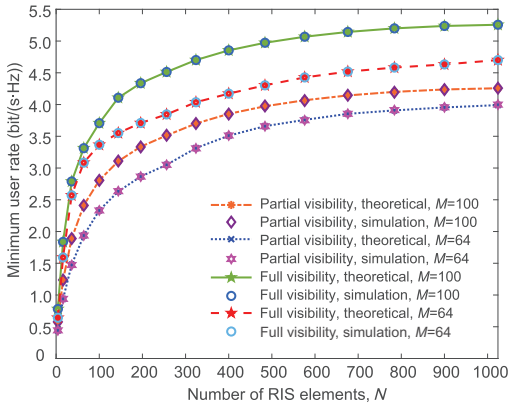

Fig. 4 Minimum user rate versus number of RIS elements (RIS: reconfigurable intelligent surface)

considering VRs. This is due to a reduction in the number of available RIS elements per user, resulting in a corresponding decline in effective array aperture and signal strength. In addition, although the VRs lead to performance degradation, it can be compensated by increasing N. For example, by analyzing Fig. 4 we can find that a partial visibility system with 400 RIS elements can outperform a full visibility system with about 100 RIS elements, assuming that the two systems have the same number of antennas. Therefore, with the help of increasing N, we can achieve the same rate as that of full visibility systems while still maintaining network capacity requirements.

Fig. 5 shows the influence of the Rician factors, indicating that the minimum user rate is a decreasing function of δ, but it is also an increasing function of ε_k. By analyzing Fig. 5, it can be concluded that as δ gradually increases, the impact of the LoS component $\bar{\boldsymbol{H}}_2$ in the RIS–BS channel is more significant.

It increases the correlation of channels between different users and intensifies MU interference, thereby reducing the spatial multiplexing gain. On the contrary, positioning the RIS at a higher elevation compared to the ground level can increase the value of ε_k. This, in turn, enhances the proportion of the LoS component $\bar{\boldsymbol{h}}_k$ in the user k–RIS channel, achieving higher system throughput as shown in Fig. 5.

In Figs. 6 and 7, we compare the minimum user rate and runtime of the gradient algorithm and GA, respectively. The analysis shows that the two algorithms have similar computational results, which proves the accuracy of the gradient algorithm. However, the runtime of GA is always longer than that of the gradient algorithm, especially when considering the VRs. This is because in the presence of spatial correlation and VRs, the objective function of the optimization problem becomes more complex and the local search ability of GA is poor, resulting in large time consumption and low search efficiency in the later stage of evolution. In this case, GA can no longer provide perfect operation results, while the gradient algorithm can still play a good role. Moreover, the efficiency of the gradient algorithm does not decrease as dramatically as GA when N is large. The reason is that the proposed gradient algorithm considers real variables of angles as optimization variables, thus avoiding performance loss caused by projection operations, and it is able to provide more stable results.

In Fig. 8, the influence of overlapping VRs is analyzed. First, it is assumed that non-overlapping means that each user's VR does not overlap with others' VR, while overlapping means that each user's VR will overlap with others' VR. It can be seen that the minimum user rate of a 100%-overlapping system is reduced by 0.1408 bits/(s·Hz) compared with a non-overlapping system, assuming $N = 1024$. Therefore, the impact of overlapping VRs on the

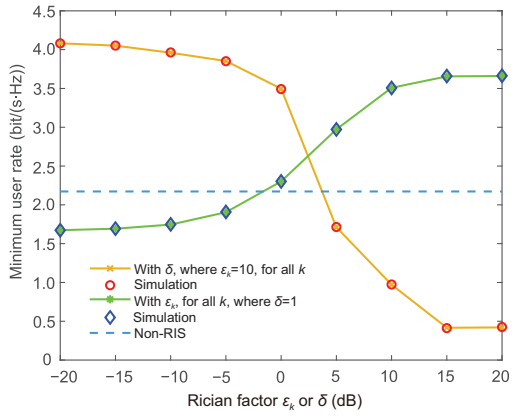

Fig. 5 Max-min achievable rate versus δ or ε_k

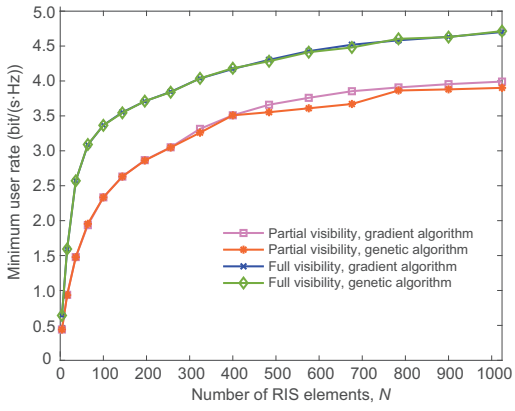

Fig. 6 Comparison of results between different optimization algorithms

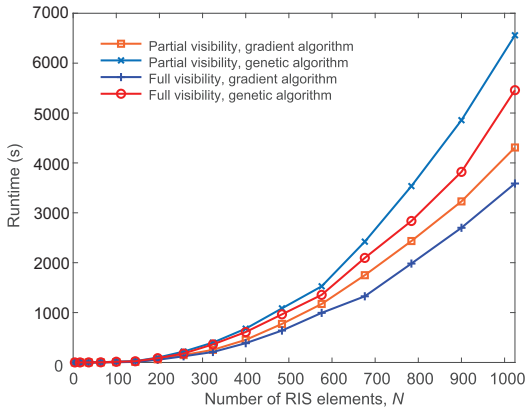

Fig. 7 Comparison of runtime between different optimization algorithms

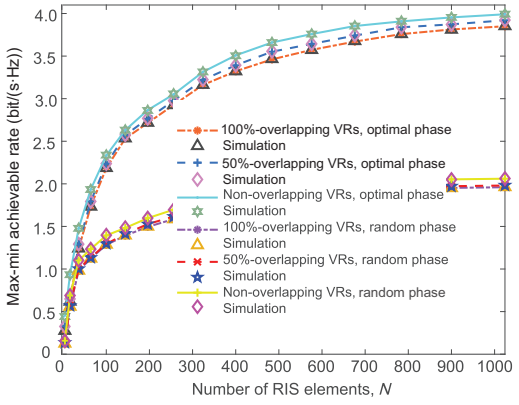

Fig. 8 Max-min achievable rate versus N for overlapping and non-overlapping VRs (VRs: visibility regions)

minimum user rate is relatively small and can be almost ignored when the rate is large. It indicates that by using the proposed phase shift optimization algorithm, the interference at overlapping VRs can be reduced. As a result, the algorithm can significantly minimize the performance gap between overlapping and non-overlapping systems, and ensure fairness in the user rate of the entire system.

Note that in this study, the objective function of the optimization problem is $f_{\mathrm{VR}}(\boldsymbol{\theta})$, and therefore spatial correlation is considered in the RIS phase shift design. From Fig. 9, it can be observed that as the spacing between RIS components decreases ($d_{\mathrm{ris}} = \lambda/2, \lambda/4, \lambda/8$), the influence of spatial correlation on the minimum user rate cannot be ignored. Specifically, for cases where N is small, the rate decreases as the element spacing decreases, which is attributed to the decrease in channel rank. For cases where N is relatively large, the channel rank still decreases. However, by increasing the number of RIS elements and using channel correlation to enhance the customized wireless channel capability provided by the RIS, the beamforming gain provided by the optimized RIS can exceed the negative impact of spatial correlation, thereby achieving higher user rates.

In Fig. 10, it can be observed that when considering the influence of RIS visibility, as N increases, the time for solving the max-min problem with the gradient algorithm also gradually increases. However, as the solution method for low-complexity rate expressions is much simpler, the runtime can be significantly reduced. Especially when N is large in XL-RIS scenarios, such as $N = 1024$, reducing complexity can increase computational speed by nearly three times.

Fig. 11 investigates the convergence behavior of the proposed low-complexity gradient algorithm compared to that of the ordinary method. By applying the proposed complexity reduction method, it can be observed that when all other conditions are the same, the number of iterations required for the low-complexity gradient algorithm to converge is always less than that of the usual gradient algorithm, and this advantage is more obvious when using the accelerated algorithm. Besides, although there is not much difference in the number of iterations before and after reducing complexity, the efficiency is significantly increased, and the total time consumption is decreased due to the greatly reduced complexity of single-iteration calculations. Moreover, the convergence speed can be further effectively improved by applying the proposed

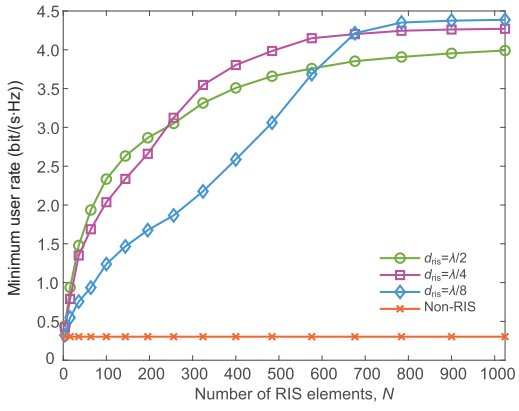

Fig. 9 Max-min achievable rate versus N for different values of the RIS element spacing d_{ris} (RIS: reconfigurable intelligent surface)

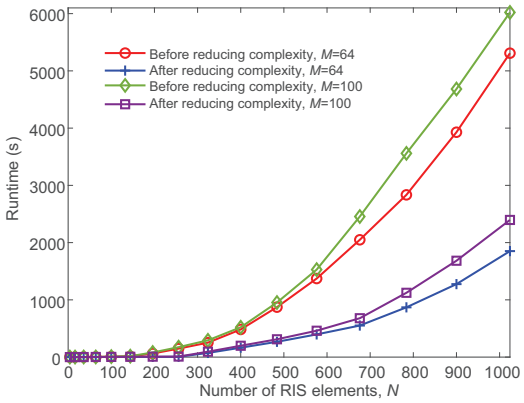

Fig. 10 Comparison of runtime before and after reducing complexity

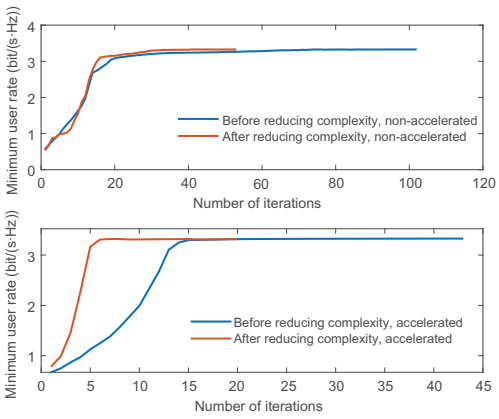

Fig. 11 Comparison of system solution iteration times before and after reducing complexity

acceleration method. Hence, the above results confirm that redundant components can be removed through the proposed method in expression (18). As a result, the achievable rate expression with dimension-reduced matrices can effectively improve system efficiency and save resources.

6 Conclusions

In this study, we studied the two-timescale design of XL-RIS-aided massive MIMO communication systems, taking into account the influence of VRs. First, we considered a spatially correlated channel model in the presence of VRs. A closed-form expression of the achievable user rate was derived and the optimization problem was clarified. At the same time, we analyzed the impact of the VR of the RIS on system complexity and simplified the user rate expression. Second, we proposed a gradient algorithm different from GA and validated the potential of applying it to the phase shift optimization problem. Finally, we conducted simulations and analysis about XL-RIS-aided massive MIMO systems, and the impact of VRs on system performance was verified from different perspectives.

Contributors

Luchu LI designed the research and drafted the paper. Cunhua PAN, Kangda ZHI, and Hong REN revised and finalized the paper.

Conflict of interest

All the authors declare that they have no conflict of interest.

Data availability

The data that support the findings of this study are available from the corresponding author upon reasonable request.

References

Abrardo A, Dardari D, Di Renzo M, 2021. Intelligent reflecting surfaces: sum-rate optimization based on statistical position information. *IEEE Trans Commun*, 69(10):7121-7136. https://doi.org/10.1109/TCOMM.2021.3096549

Ali A, Carvalho ED, Heath RW, 2019. Linear receivers in non-stationary massive MIMO channels with visibility regions. *IEEE Wirel Commun Lett*, 8(3):885-888. https://doi.org/10.1109/LWC.2019.2898572

Björnson E, Sanguinetti L, 2021. Rayleigh fading modeling and channel hardening for reconfigurable intelligent surfaces. *IEEE Wirel Commun Lett*, 10(4):830-834. https://doi.org/10.1109/LWC.2020.3046107

Cao YS, Lv TJ, Ni W, 2022. Two-timescale optimization for intelligent reflecting surface-assisted MIMO transmission in fast-changing channels. *IEEE Trans Wirel Commun*, 21(12):10424-10437. https://doi.org/10.1109/TWC.2022.3184000

Carvalho ED, Ali A, Amiri A, et al., 2020. Non-stationarities in extra-large-scale massive MIMO. *IEEE Wirel Commun*, 27(4):74-80. https://doi.org/10.1109/MWC.001.1900157

Chen TR, You ML, Zhang YYS, et al., 2024. Model-free optimization and experimental validation of RIS-assisted wireless communications under rich multipath fading. *IEEE Wirel Commun Lett*, 13(3):627-631. https://doi.org/10.1109/LWC.2023.3337709

Cui MY, Dai LL, 2022. Channel estimation for extremely large-scale MIMO: far-field or near-field? *IEEE Trans Commun*, 70(4):2663-2677. https://doi.org/10.1109/TCOMM.2022.3146400

Gan X, Zhong CJ, Huang CW, et al., 2022. Multiple RISs assisted cell-free networks with two-timescale CSI: performance analysis and system design. *IEEE Trans Commun*, 70(11):7696-7710. https://doi.org/10.1109/TCOMM.2022.3208629

Gao YW, Xu JD, Xu W, et al., 2021. Distributed IRS with statistical passive beamforming for MISO communications. *IEEE Wirel Commun Lett*, 10(2):221-225. https://doi.org/10.1109/LWC.2020.3024952

Gunasinghe D, Amarasuriya G, 2023. Achievable rate analysis for extra-large RIS-aided massive MIMO with visibility regions. IEEE Int Conf on Communications, p.1542-1547. https://doi.org/10.1109/ICC45041.2023.10279151

Guo YB, Sun P, Yuan ZD, et al., 2023. Efficient channel estimation for RIS-aided MIMO communications with unitary approximate message passing. *IEEE Trans Wirel Commun*, 22(2):1403-1416. https://doi.org/10.1109/TWC.2022.3204688

Han Y, Tang WK, Jin S, et al., 2019. Large intelligent surface-assisted wireless communication exploiting statistical CSI. *IEEE Trans Veh Technol*, 68(8):8238-8242. https://doi.org/10.1109/TVT.2019.2923997

Han Y, Jin S, Wen CK, et al., 2022. Localization and channel reconstruction for extra large RIS-assisted massive MIMO systems. *IEEE J Sel Top Signal Process*, 16(5):1011-1025. https://doi.org/10.1109/JSTSP.2022.3174654

Hu C, Dai LL, Han SF, et al., 2021. Two-timescale channel estimation for reconfigurable intelligent surface aided wireless communications. *IEEE Trans Commun*, 69(11):7736-7747. https://doi.org/10.1109/TCOMM.2021.3072729

Huang CW, Hu S, Alexandropoulos GC, et al., 2020. Holographic MIMO surfaces for 6G wireless networks: opportunities, challenges, and trends. *IEEE Wirel Commun*, 27(5):118-125. https://doi.org/10.1109/MWC.001.1900534

Jaynes ET, 1957. Information theory and statistical mechanics. *Phys Rev*, 106(4):620-630. https://doi.org/10.1103/PhysRev.106.620

Jia YH, Ye CC, Cui Y, 2020. Analysis and optimization of an intelligent reflecting surface-assisted system with interference. IEEE Int Conf on Communications, p.1-6. https://doi.org/10.1109/ICC40277.2020.9148666

Jiang H, Xiong BP, Zhang HM, et al., 2023. Physics-based 3D end-to-end modeling for double-RIS assisted non-stationary UAV-to-ground communication channels. *IEEE Trans Commun*, 71(7):4247-4261. https://doi.org/10.1109/TCOMM.2023.3266832

Li RW, Sun S, Chen YH, et al., 2023. Ergodic achievable rate analysis and optimization of RIS-assisted millimeter-wave MIMO communication systems. *IEEE Trans Wirel Commun*, 22(2):972-985. https://doi.org/10.1109/TWC.2022.3199991

Li XR, Zhou SD, Björnson E, et al., 2015. Capacity analysis for spatially non-wide sense stationary uplink massive MIMO systems. *IEEE Trans Wirel Commun*, 14(12):7044-7056. https://doi.org/10.1109/TWC.2015.2464219

Li XS, 1992. An entropy-based aggregate method for minimax optimization. *Eng Optim*, 18(4):277-285. https://doi.org/10.1080/03052159208941026

Liu YW, Xu JQ, Wang ZL, et al., 2023. Simultaneously transmitting and reflecting (STAR) RISs for 6G: fundamentals, recent advances, and future directions. *Front Inform Technol Electron Eng*, 24(12):1689-1707. https://doi.org/10.1631/FITEE.2300490

Marzetta TL, Larsson EG, Yang H, et al., 2016. Fundamentals of Massive MIMO. Cambridge University Press, Cambridge, UK. https://doi.org/10.1017/CBO9781316799895

Pan CH, Ren H, Wang KZ, et al., 2021. Reconfigurable intelligent surfaces for 6G systems: principles, applications, and research directions. *IEEE Commun Mag*, 59(6):14-20. https://doi.org/10.1109/MCOM.001.2001076

Pan CH, Zhou G, Zhi KD, et al., 2022. An overview of signal processing techniques for RIS/IRS-aided wireless systems. *IEEE J Sel Top Signal Process*, 16(5):883-917. https://doi.org/10.1109/JSTSP.2022.3195671

Peng ZD, Pan CH, Zhou G, et al., 2023. Two-stage channel estimation for RIS-aided multiuser mmWave systems with reduced error propagation and pilot overhead. *IEEE Trans Signal Process*, 71:3607-3622. https://doi.org/10.1109/TSP.2023.3317729

Ren H, Liu XY, Pan CH, et al., 2023. Performance analysis for RIS-aided secure massive MIMO systems with statistical CSI. *IEEE Wirel Commun Lett*, 12(1):124-128. https://doi.org/10.1109/LWC.2022.3218961

Tang WK, Chen MZ, Chen XY, et al., 2021. Wireless communications with reconfigurable intelligent surface: path loss modeling and experimental measurement. *IEEE Trans Wirel Commun*, 20(1):421-439. https://doi.org/10.1109/TWC.2020.3024887

Wang JH, Wang HQ, Han Y, et al., 2021. Joint transmit beamforming and phase shift design for reconfigurable intelligent surface assisted MIMO systems. *IEEE Trans Cogn Commun Netw*, 7(2):354-368. https://doi.org/10.1109/TCCN.2021.3058665

Wang XH, Shu F, Chen RQ, et al., 2023. Beamforming design for RIS-aided amplify-and-forward relay networks. *Front Inform Technol Electron Eng*, 24(12):1728-1738. https://doi.org/10.1631/FITEE.2300118

Wang ZR, Liu L, Cui SG, 2020. Channel estimation for intelligent reflecting surface assisted multiuser communications: framework, algorithms, and analysis. *IEEE Trans Wirel Commun*, 19(10):6607-6620. https://doi.org/10.1109/TWC.2020.3004330

Wei XH, Dai LL, Zhao YJ, et al., 2022. Codebook design and beam training for extremely large-scale RIS: far-field or near-field? *China Commun*, 19(6):193-204. https://doi.org/10.23919/JCC.2022.06.015

Xu DN, Han Y, Li X, et al., 2023. Energy efficiency optimization for a RIS-assisted multi-cell communication system based on a practical RIS power consumption model. *Front Inform Technol Electron Eng*, 24(12):1717-1727. https://doi.org/10.1631/FITEE.2300136

Yang L, Meng FX, Zhang JY, et al., 2020a. On the performance of RIS-assisted dual-hop UAV communication systems. *IEEE Trans Veh Technol*, 69(9):10385-10390. https://doi.org/10.1109/TVT.2020.3004598

Yang L, Yang JX, Xie WW, et al., 2020b. Secrecy performance analysis of RIS-aided wireless communication systems. *IEEE Trans Veh Technol*, 69(10):12296-12300. https://doi.org/10.1109/TVT.2020.3007521

Yang L, Yang Y, da Costa DB, et al., 2021. Outage probability and capacity scaling law of multiple RIS-aided networks. *IEEE Wirel Commun Lett*, 10(2):256-260. https://doi.org/10.1109/LWC.2020.3026712

Yang SJ, Lyu W, Xiu Y, et al., 2023. Active 3D double-RIS-aided multi-user communications: two-timescale-based separate channel estimation via Bayesian learning. *IEEE Trans Commun*, 71(6):3605-3620. https://doi.org/10.1109/TCOMM.2023.3265115

Yu X, Shen WQ, Zhang R, et al., 2023. Channel estimation for XL-RIS-aided millimeter-wave systems. *IEEE Trans Commun*, 71(9):5519-5533. https://doi.org/10.1109/TCOMM.2023.3286450

Zhang Q, Lu ZH, Jin S, et al., 2013. Power scaling of massive MIMO systems with arbitrary-rank channel means and imperfect CSI. IEEE Global Communications Conf, p.4157-4162. https://doi.org/10.1109/GLOCOM.2013.6831725

Zhang Y, 2023. Reconfigurable intelligent surfaces for 6G: applications, challenges, and solutions. *Front Inform Technol Electron Eng*, 24(12):1669-1688. https://doi.org/ 10.1631/FITEE.2200666

Zheng BX, You CS, Zhang R, 2021. Double-IRS assisted multi-user MIMO: cooperative passive beamforming design. *IEEE Trans Wirel Commun*, 20(7):4513-4526. https://doi.org/10.1109/TWC.2021.3059945

Zhi KD, 2023. Two-Timescale Design for RIS-Aided Massive MIMO Systems. PhD Thesis, Queen Mary University of London, UK.

Zhi KD, Pan CH, Ren H, et al., 2022a. Active RIS versus passive RIS: which is superior with the same power budget? *IEEE Commun Lett*, 26(5):1150-1154. https://doi.org/10.1109/LCOMM.2022.3159525

Zhi KD, Pan CH, Ren H, et al., 2022b. Power scaling law analysis and phase shift optimization of RIS-aided massive MIMO systems with statistical CSI. *IEEE Trans Commun*, 70(5):3558-3574. https://doi.org/10.1109/TCOMM.2022.3162580

Zhi KD, Pan CH, Ren H, et al., 2023. Two-timescale design for reconfigurable intelligent surface-aided massive MIMO systems with imperfect CSI. *IEEE Trans Inform Theory*, 69(5):3001-3033. https://doi.org/10.1109/TIT.2022.3227538

Zhi KD, Pan CH, Ren H, et al., 2024. Performance analysis and low-complexity design for XL-MIMO with near-field spatial non-stationarities. *IEEE J Sel Areas Commun*, 42(6):1656-1672. https://doi.org/10.1109/JSAC.2024.3389128

Zhou G, Pan CH, Ren H, et al., 2022. Channel estimation for RIS-aided multiuser millimeter-wave systems. *IEEE Trans Signal Process*, 70:1478-1492. https://doi.org/10.1109/TSP.2022.3158024

Zhou SQ, Xu W, Wang KZ, et al., 2020. Spectral and energy efficiency of IRS-assisted MISO communication with hardware impairments. *IEEE Wirel Commun Lett*, 9(9):1366-1369. https://doi.org/10.1109/LWC.2020.2990431

List of supplementary materials